# Flow of the partially molten crust in the Variscan foreland revealed by U–Th–Pb dating of metamorphism, magmatism and deformation (Agly Massif, Eastern Pyrenees)

J. Vanardois, P. Trap, F. Roger, P. Goncalves, D. Marquer, J. Paquette, G. Siron, Thierry Baudin

# *Flow of the partially molten crust in the Variscan foreland revealed by U-Th-Pb dating of metamorphism, magmatism and deformation (Agly Massif, eastern Pyrenees).*

Vanardois[1*] J., Trap[1] P., Roger[2] F., Goncalves[1] P., Marquer[1] D., Paquette[3] JL., Siron[4] G., Baudin[5] T.

jonas.vanardois@univ-fcomte.fr; pierre.trap@univ-fcomte.fr; francoise.roger@umontpellier.fr; philippe.goncalves@univ-fcomte.fr; didier.marquer@univ-fcomte.fr; j.l.paquette@opgc.univ-bpclermont.fr; siron@wisc.edu ; t.baudin@brgm.fr

[1]UMR 6249 Chrono-environnement, Université de Bourgogne-Franche-Comté, 25030 Besançon, France.

[2]Géosciences Montpellier, Campus Triolet, Université Montpellier, CNRS, 34095 Montpellier Cedex 5, France.

[3]Laboratoire Magmas et Volcans (CNRS-UMR 6524), Campus Universitaire des Cézeaux, 63178 Aubière Cedex, France.

[4]WiscSIMS Laboratory, University of Wisconsin-Madison, Madison, Wisconsin 53706, United States of America.

[5]BRGM-French Geological Survey, 3 Avenue Claude Guillemin, 45100, Orléans, France.

*Corresponding author: jonasvanardois@gmail.com +33(0)606755562; Present address: 16 route de Gray, 25030 Besançon.

**Keywords**: Crustal flow, Strain partitioning Variscan orogen, Agly Massif, LA-ICPMS U-Th-Pb dating

## Abstract

In this contribution, we investigate the spatial and temporal evolution of mid-crustal flow in the Agly massif (North Pyrenean Zone) that represents the southern foreland of the Variscan orogenic plateau. In the Agly massif, the middle crust is represented by an Ediacarian-Devonian series of metasedimentary rocks that recorded high-grade metamorphism synchronously with crustal thinning (D2) and dextral wrenching (D3) during Carboniferous. D2 crustal thinning formed a penetrative S2 flat-lying foliation and localized C2 extensional shear zones with a top-to-the-North kinematics. D2 planar fabrics are deformed by a D3 dextral transpression localized into a two-kilometers wide high-strain zone. We performed LA-ICPMS U-Th-Pb dating on zircon and monazite from small magmatic bodies and from metamorphic rocks showing strain features relative to D2 and/or D3. Our results, compiled with published data, argue that the middle crust of the Agly massif reached high-temperature and suprasolidus conditions at ca. 325-320 Ma and was partially molten until ca. 300 Ma. They also indicate that the D2 thinning and top-to-the north shearing was active from ca. 325 to 290 Ma. D2 extension and D3 transpression were synchronous from ca. 308 to 290 Ma. Making a comparison with the Pyrenean Axial Zone, the Montagne Noire and the French Central massif, we propose a two-step tectonic model for the mid-crustal flow with a horizontal flow towards South in both the orogenic plateau and the southern forelands between ca. 325 and 310 Ma and locally reoriented into an E-W longitudinal flow between 310 and 300 Ma in high-strain dextral strike-slip shearing domains.

## Introduction

The Variscan belt is considered as an ancient analogue of large and hot orogens (e.g. Maierova et al. 2016). As such, it constitutes a natural laboratory to observe deep crustal flow mechanisms (e.g. Schulmann et al. 2008), as those currently operating beneath the Andean (e.g. Gerbault et al. 2005) and Tibetan orogenic plateau (e.g. Clarck and Royden 2000). In the French Variscan belt, the occurrence of eclogite boudins hosted in migmatites exhumed in the foreland has been interpreted as an evidence for southward horizontal flow of the partially molten lower crust (Fig. 1, Whitney et al. 2015, Pitra et al. 2021). In the eastern part of the French Massif Central, the southward rejuvenation of partial melting and the progressive evolution of crustal-derived plutonic rocks from ca. 345 Ma to ca. 310 Ma (Laurent et al. 2017) is attributed to a southward horizontal growth of the Variscan belt and formation of an orogenic plateau by gravity-driven lateral flow of the partially molten orogenic root (Vanderhaeghe et al. 2020).. Later structures are dominantly interpreted as a late-orogenic gravitational collapse recorded between 305 and 290 Ma (e.g. Rey et al. 2011, 2017; Vanderhaeghe et al. 2020 and references therein).

In addition, the Carboniferous building of the Variscan belt was widely impacted by the development of crustal-scale strike-slip shear zones (e.g. Carreras and Druguet 2014; Franke et al. 2017; Chardon et al. 2020; Edel et al. 2018 and references therein). It is far from being clear to what extent the gravity-driven lateral flow and the strike-slip-controlled longitudinal or extrusional flow interacted in the partially molten orogenic root. Accurate dating of melting and solid-state deformation, as well as characterization of feedback relationship between plutonism and crustal-scale shear zones are still needed to understand the flow dynamics of partially molten crust.

The North-Pyrenean-Zone (NPZ, Fig. 1) represents the southern foreland of the Variscan belt where the partially molten orogenic root might have flowed southwards (Whitney et al. 2015; Vanderhaeghe et al. 2020). In comparison with the hinterland areas, the NPZ still lacks precise geochronological data that are required to date deformation and fully understand the flow pattern of the partially molten crust in the external portion of the Variscan orogenic plateau. At the eastern edge of the NPZ, the Agly massif shows a finite strain pattern that results from the superposition of flat-lying and vertical foliations related to bulk thinning and dextral wrenching, respectively. Based on U-Th-Pb zircon dating of plutons (Olivier et al. 2004, 2008; Tournaire Guille et al. 2019) and their relationships with the deformation phases, Vanardois et al. (2020) proposed that the flat-lying structure (D2) and wrench-related vertical structures (D3) may have been partially coeval. In this contribution, we performed LA-ICPMS U-Th-Pb dating on zircon and monazite from pegmatites, leucogranites and metamorphic rocks (i.e. orthogneiss and paragneiss) in order to constrain the timing of D2 thinning and D3 wrenching, and associated metamorphism and magmatism. These new geochronological results compared with structural and metamorphic data allow us to discuss the strain partitioning evolution in space and time during middle crustal flow of the Variscan belt foreland.

## Geological Setting

The Variscan Pyrenees are located in the external domain of the Variscan belt and represent its southern orogenic foreland (Druguet 2001; Edel et al. 2018; Laurent et al. 2017; Aguilar et al. 2013; Martinez-Catalan et al., 2021) (Fig. 1a). The Pyrenean Axial Zone (PAZ) and the North Pyrenean Zone (NPZ) are separated by the EW-striking North Pyrenean Fault (NPF). These two zones consist of Proterozoic to Paleozoic sedimentary rocks deformed and metamorphosed between the middle Carboniferous and the early Permian (Mezger and Gerdes 2016; Denèle et al. 2014; Aguilar et al. 2013; Schnapperelle et al. 2020; Vacherat et al. 2017; Cochelin et al. 2021; Cugerone et al. 2021; Vielzeuf et al. 2021). In both PAZ and NPZ, the Variscan orogeny is associated with a widespread Carboniferous to Permian magmatism (e.g. Denèle et al. 2014; Pereira et al. 2014; Druguet et al. 2014; Lemirre 2016; Vacherat et al. 2017; Lemirre et al. 2019).

In the NPZ, few relics of kyanite have been described (Fonteilles et al. 1964; Fonteilles 1970; Fonteilles and Guitard 1971) leading some authors to propose an early thickening event (D1) related to nappe stacking (e.g. Bouhallier et al. 1991; Olivier et al. 2004). LA-ICPMS U-Th-Pb ages at ca. 325-320 Ma obtained in the NPZ are interpreted as the onset of partial melting during D1 prior to the pervasive high temperature and low-pressure event (M2) widely recorded in the Pyrenees (Lemirre 2016). This high temperature event is coeval with the widespread development of sub-horizontal foliation, interpreted as the result of extensional collapse (D2) during late Carboniferous (Bouhallier et al. 1991; de Saint-Blanquat 1993; Vanardois et al. 2020).

At the eastern edge of the NPZ, the Agly massif forms a WNW-ESE trending, 30 km long and 10 km wide Variscan massif that was exhumed during Cretaceous extension and subsequent Tertiary Pyrenean continental collision. The Agly massif is composed of a Proterozoic to Devonian metasedimentary sequence (Fonteilles 1970; Berger et al. 1993) that contains sills of Cambrian (ca. 540 Ma) and Ordovician (ca. 450 Ma) orthogneisses (Tournaire Guille et al. 2019; Paquette et al. 2021).

The metasedimentary sequence is classically subdivided into an infrastructure and a suprastructure (Fonteilles 1970). The suprastructure consists of unmolten metasedimentary rocks represented by

Cambrian to Ordovician micaschists and schists, Silurian black-schists and Devonian marbles (Fig. 2) with few metric quartzite layers. The suprastructure is characterized by a HT-LP metamorphic gradient of ~55°C/km (Vielzeuf 1984; Andrieux 1982a, 1982b; Delay 1989; Bouhallier et al. 1991; Siron et al. 2020) with a maximum temperature of 680°C at its base (Siron et al. 2020; Bouhallier et al. 1991; Delay 1989). The infrastructure is composed of partially molten metapelites, metagreywackes, calc-silicates,marbles and meta-igneous rocks, the latter being mainly orthogneissified (Fig. 2). Siron et al. (2020) have shown that the infrastructure is characterized by a near isothermal gradient buffered at around 740-790°C between 0.5 and 0.66 GPa. LA-ICPMS U-Th-Pb monazite dating of two high-aluminium pelitic samples (kinzigites) estimated the peak of the HT-LP metamorphism at ca. 305 Ma (Siron et al. 2020). Several 100-meter thick, flat-lying mylonitic shear zones are documented in the infrastructure, together with the main Caladroy shear zone (CSZ) that is located near the anatectic front (Delay et al. 1989; Bouhallier et al. 1991; Siron et al. 2020; Vanardois et al. 2020) (Fig. 3a). The CSZ separates the infra- and suprastructure (Vanardois et al. 2020) and subtracted about 5 km of crustal material (Delay 1989; Bouhallier et al. 1991; Siron et al. 2020).

Several Carboniferous magmatic rocks intruded at different levels into the infra- and supra-structures. The Ansignan pluton is a 500 meter-thick charnockitic laccolith emplaced in the deepest part of the infrastructure, with smaller satellite sills observed in the southern part of the massif (Fig. 2) (Delay 1989; Fonteilles et al. 1993). The Ansignan pluton is concordant with the layering of the surrounding migmatitic gneisses (Althoff et al., 1994; Vanardois et al. 2020) and consists of three facies: (i) a melanocratic K-feldspar porphyric, garnet and orthopyroxene-bearing granodiorite, (ii) a garnet-bearing leucogranite and (iii) mafic enclaves (Berger et al. 1993; Delay 1989; Althoff et al. 1994; Olivier et al. 2008). These three facies have been dated by U-Pb method by ID-TIMS on zircon and monazite and yielded ages between 315 and 290 Ma (Postaire 1982; Respaut and Lancelot 1983). The most recent age at 307 ± 3 Ma (U-Th-Pb LA-ICPMS on zircon) was interpreted by Tournaire Guille et al. (2019) as the emplacement age of the Ansignan charnockite. However, these same authors also obtained on a mylonitized charnockitic sill two concordia ages, one at 313.9 ± 2.9 Ma on zircon cores and the other at 298.6 ± 2.7 Ma on zircon rims, without really interpreting them. The Cassagnes granite occurs as a set of few meter-thick sills in the infrastructure located, near the Cassagnes village (Fig. 2). It is a melanocratic K-feldspar phenocrysts, garnet-bearing granodiorite, very similar to the Ansignan charnockite except that orthopyroxene is rare, and it was emplaced at 308 ± 3 Ma (U-Pb LA-ICPMS on zircon; Tournaire et al. 2019). The emplacement of a monzogranitic sill into the infrastructure has been dated by upper intercept at 317 ± 3 Ma (ID-TIMS on zircon; Olivier et al. 2004), but a few years later Olivier et al. (2008) interpreted this age as a mixing date between inherited cores and Variscan rims.

The suprastructure is intruded by the Tournefort diorite and the Saint-Arnac pluton (Fig. 2). The Tournefort diorite has been dated by upper intercept at 308 ± 1 Ma and by a concordia age at 307 ± 1 Ma (ID-TIMS on zircon; Olivier et al. 2004, 2008). The southern part of the Saint-Arnac pluton is composed of several granitic facies partly mingled with dioritic facies that may be cogenetic with the Tournefort diorite (Olivier et al. 2008). On the southern edge of the Saint-Arnac pluton, the age of the granodiorite has been dated by upper intercept at 304 ± 5 Ma (ID-TIMS on zircon; Olivier et al. 2008) and by weighted mean $^{206}Pb/^{238}U$ dates at 308 +4/-2 Ma (LA-ICPMS on zircon; Odlum and Stockli 2019), whereas the zircons from the northern edge of the pluton yield a mean $^{206}Pb/^{238}U$ age of 301 +3/-2 Ma (LA-ICPMS; Odlum and Stockli 2019). Numerous meter-sized pegmatitic and leucogranitic dykes and sills intruded the infra- and supra-structures and the plutons.

The main penetrative strain pattern is related to the D2 deformation event defined by a pervasive flat-lying foliation S2 (Vanardois et al. 2020). D2 reworked an early vertical N-S trending foliation attributed to the D1 thickening event (Fig. 3 and 4a-b, Vanardois et al. 2020). The D2 deformation was coeval with the HT/LP M2 metamorphism, migmatization, and the Ansignan and Cassagnes intrusions (Delay 1989; Paquet and Mansy 1991; Bouhallier et al. 1991; Althoff et al. 1994, Vanardois et al. 2020). D2 deformation continued during retrogressed conditions and formed C2 extensional shear zones (Fig. 3 and 4c-d) responsible for the bulk thinning of the Agly massif. The Caladroy shear zone (CSZ), separating the infra- and suprastructure, is one of these C2 shear zones (Fig. 3). The evolution of D2 from suprasolidus S2 foliations to subsolidus C2 strain localization (Vanardois et al., 2020) is defined in the following sections as S2 and C2 structures, respectively. Siron et al. (2020) documented LA-

ICPMS U-Th-Pb ages at ca. 296-300 Ma from monazite overgrowths of a C2 mylonite, interpreted as the timing of late D2 crustal thinning.

In the northern part of the Agly massif, Vanardois et al. (2020) described a third deformation phase D3 corresponding to a dextral transpression localized along an E-W 2 km-wide corridor (Fig. 3 TDZ). This D3 corridor shows a prominent vertical foliation S3 that reworked former D2 (S2 and C2) planar fabrics (Fig. 3 and 4e-f). The D3 event is subdivided into an early transtensional deformation, named proto-D3 and a late transpressional regime D3 sensu stricto, named Late-D3 (Vanardois et al. 2020). The D3 corridor acted as preferential pathways for upward migration of the Tournefort diorite and Saint-Arnac granite magmas (Vanardois et al. 2020).

The Tertiary Pyrenean tectonics is characterized in the Agly massif by brittle deformation with steep reversed faults affecting the Variscan basement and Mesozoic rocks. This last stage is affected by N020 and N150 striking conjugate strike-slip faults accommodating the N-S Pyrenean compression.

## U-Th-Pb geochronology

In this study, we report new zircon and monazite U-Th-Pb dates from nine rock samples from the Agly massif corresponding to syn-tectonic granitoids or mylonitic rocks have been collected with respect to the main deformation events and their location in the infra- or suprastructure (Fig. 2 and 3 and Table 1 for locations). (i) Samples Ag57 and Ag3B are located in S2 strain domains. Sample Ag57 is an undeformed leucogranitic sill located in the western part of the Agly massif in the deepest part of the infrastructure. The sample Ag3B is a migmatitic paragneiss located in the upper part of the infrastructure, (ii) Samples Ag38, Ag03 and Ag47 are pegmatites located within the C2 shear zones. Two of them are located within the CSZ at the infra- and suprastructure boundary, one pegmatite is deformed (Ag38), the other is slightly deformed (Ag03). The pegmatite Ag47 is located in the suprastructure and is mylonitized by a C2 shear zone. (iii) Samples Ag08 and Ag06 are two dykes that crosscut the Proto-D3 transtensional structures from the Tournefort area. One is a pegmatite located in the Tournefort diorite (Ag08), the other is a leucogranite emplaced near the Saint-Arnac pluton (Ag06). (iv) Sample Ag48 is a migmatitic orthogneiss from the infrastructure located in the Late-D3 transpressional structures of the D3 corridor while Ag51 is a leucogranite collected within the axial plane of a late-D3 fold at the vicinity of the D3 corridor. Samples presentations are detailed in the followings.

**Analytical method**

Monazite and zircon were obtained by standard crushing and heavy liquid and magnetic separation using Frantz isodynamic techniques. The crystals were handpicked under a binocular microscope, then mounted in epoxy resin discs and polished to expose mid-grain sections. One exception is monazite from sample Ag3B that was analysed in-situ (thin section) to preserve textural relationships, the rock-forming mineralogical assemblage and the fabrics. Cathodoluminescence (CL) and backscattered electrons (BSE) images were used to select points for analysis (Fig. S1 and S2, supplementary material). U-Th-Pb geochronology of zircon and monazite was obtained by laser ablation inductively coupled plasma spectrometry (LA-ICPMS) at the Laboratoire Magmas et Volcans (Clermont-Ferrand, France). The analysis involved the ablation of minerals with a Resonetics Resolution M-50 powered by an ultra-short pulse ATL Atlex Excimer laser system operating at a wavelength of 193 nm. For zircon and monazite, spot diameters of 27 µm or 33 µm and 12 µm were used, associated with repetition rates of 3 Hz and 1 Hz, and laser fluences of 4J/cm2 and 9J/cm2 respectively. The ablated material was carried by helium and then mixed with nitrogen and argon before injection into the plasma source of an Agilent 7500 cs ICP-MS equipped with a dual pumping system to enhance sensitivity (Paquette et al. 2014). The detailed analytical procedures are described in Paquette and Tiepolo (2007), Hurai et al. (2010), Paquette et al. (2014) and in the supplementary material (Table S1). Data reduction was carried out with the GLITTER® software package from Macquarie Research Ltd (Van Achterbergh et al. 2001). Calculated ratios were exported and ages and diagrams were generated using Isoplot/Ex v. 2.49 software package of Ludwig (2001). In the text and figures, all uncertainties in ages are given at the $\pm 2\sigma$ level. The decay constants used for the U-Th-Pb system are those determined by Jaffey et al. (1971) and recommended by IUGS (Steiger and Jäger 1977). Analytical results are given in Tables S2 and S3 (supplementary material). Monazite data by LA-ICPMS were plotted in a U-Th-Pb modified concordia diagram ($^{206}Pb/^{238}U$ vs $^{208}Pb/^{232}Th$) because $^{232}Th$ measurement is more accurate than $^{235}U$.

## Samples from S2 strain domains

*The Vivier deformed leucogranite (Ag57)*

The Vivier leucogranite (Ag57) is a two-meter-thick magmatic sill composed of Qtz + Kfs + Pl ± Grt ± Bt. The sill is sub-horizontal, undeformed and parallel with the surrounding S2 foliation. Most of the analysed monazite crystals in sample Ag57 are round-shaped, translucent to slightly opaque and yellow. BSE images of some monazite grains show a simple growth zoning (Fig. S1). Twenty-nine analyses were performed on nineteen monazite crystals (Fig. 5a; Table S2). Unlike Pb concentrations (1356-2152 ppm), Th and U contents vary significantly between different crystals or different domains within a single crystal. Th and U contents range from 18394 to 75616 ppm and 1847 to 11425 ppm, respectively. Th/U ratios are between 1.6 and 33.5 (Table S2). All these data are concordant between 280 and 320 Ma and, excluding two analyses (dotted ellipses), yield a concordia age of 298.9 ± 1.9 Ma ($MSWD_{(C+E)}$ = 1.7; n = 26) (Fig. 5a).

The analysed zircon crystals are transparent, colourless and slightly rounded. CL imaging shows complex internal textures with the systematic occurrence of inherited core displaying either a typical magmatic concentric oscillatory zoning or patchy zoning textures surrounded by rims (Fig. S2). Forty-five analyses were performed on thirty zircon grains (Table S3). Among these data, thirty-seven are concordant but scattered along the concordia curve between around 700 to 300 Ma and form two distinct clusters: a scattered population between 700 and 450 Ma (group 1) and a range of dates between 350 and 300 Ma (group 2) (Fig. 5b; Table S3). The single-analysis concordia ages histogram suggests that the group 1 data are distributed among at least two main populations, one at 630-710 Ma and the other at 550-610 Ma, with perhaps a third minor around ca. 450 Ma (Table S3; Fig. 5b). The oldest peak is defined by 13 data (9 cores and 4 rims, Table S3) characterized by Th contents ranging from 13 to 254 ppm, with Th/U from 0.11 to 1.77 (most >0.3), these values are typical of magmatic zircon (Tiepel et al., 2004; Linnemann et al., 2011) (Table S3). The dates range from 637 ± 19 Ma to 709 ± 20 Ma with a weighted average of single-analysis concordia ages of 671 ± 15 (MSWD = 6.3; n =13). The next peak is also composed of 13 data (9 rims and 4 cores, S3) that have Th concentrations between 19-347 ppm with the Th/U ratios ranging from 0.14-1.22 except for three rims (Th/U = 0.02-0.04) (Table S3). These dates are between 550 ± 16 Ma and 608 ± 18 Ma with a weighted average of single-analysis concordia ages of 578 ± 13 Ma (MSWD = 6.1; n =13) (Fig. 5b).

The youngest cluster (group2) is defined by 8 rim data including 5 concordant ones showing Th contents between 3 and 17 ppm (except for one at 196 ppm) and low Th/U ratios of 0.01-0.08 (except for one at 0.38) (Table S3; Fig. 5b). Among the five concordant dates, three (Zr27b, Zr43b, Zr41b) yield a concordia age of 339.5 ± 13 Ma ($MSWD_{(C+E)}$ = 2.8) and the two youngest data (Zr57b, Zr44b) give a concordia age of 305.8 ± 6.8 Ma ($MSWD_{(C+E)}$ = 0.23). This date is consistent with the lower intercept date obtained by the linear regression on the 4 youngest data (2 concordant and 2 discordant data (Zr20b, Zr42b)) of 305.1 ± 7.8 Ma (MSWD = 0.16). Other data (dotted ellipses) are not taken into account because they are discordant probably due to radiogenic lead loss and common Pb contamination (Fig. 5b).

*The migmatitic paragneiss from the Agly dam (Ag3B)*

Ag3B is a migmatitic paragneiss sampled near the Agly dam composed of Kfs + Qtz leucosomes and Bt + Sill melanosomes, both containing garnet (Fig. 6a). It is located in the upper structural levels of the infrastructure, close to the southern boundary of the D3 corridor (Fig. 3). Small C2 shear zones are located in the melanosomes whereas the leucosomes are weakly deformed. Garnets are elongated and fractured parallel to the S2 foliation. Thus, we suggest that melting and subsequent leucosome crystallization occurred earlier than the C2 event.

Monazite crystals from this sample (Ag3B) have been analysed in a thin section in order to preserve textural relationships. Monazite occurs both in the Qtz-Kfs matrix (e.g. Mn7; Mn19, Fig. 6b), as inclusions in the elongated and fractured garnet (e.g. Mn5; Mn10, Fig. 6c and d) and in Bt-Sill shear band (e.g. Mn9; Mn16, Fig. 6e and f). In relation to their textural position, thirty-seven analyses on thirty monazite grains have been performed (Table S2). High to very high Pb, Th and U contents of matrix-monazite or inclusion-monazite inclusion are similar with very wide ranges between 1084-3782 ppm (most 1084-2879 ppm), 35693-118463 ppm (most 35693–80990 ppm) and 1587–13134 ppm, respectively. The Th/U ratios are between 3.8 and 29.9. The highest ratios are found in some monazite grains included in the garnet (Table S2).

The three matrix-monazite grains analysed (Mn 7, 18 and 19) are anhedral small grains (30 to 60 µm) without clear zonation (Fig. 6b). These analyses yield a concordia age of 292 ± 4 Ma ($MSWD_{(C+E)}$ = 1.8; n = 3; Fig. 7a).

Ten monazite inclusions within garnet (Mn 10, 41, 39, 28, 5, 27, 2, 1, 24 and 26) are anhedral and 50-150 µm in size with sometimes slight patchy zoning in BSE (Fig. 6c and d). They are present in garnet from core to rim and thus grew before or synchronously with garnet crystallization. However, the well-known armouring effect of garnet (e.g. Goncalves et al., 2004; Dumond et al., 2015) is limited by the presence of numerous fractures that may have favoured fluid-assisted dissolution-precipitation of monazite after garnet crystallization. The thirteen analyses yield an upper intercept date of 295 ± 8 Ma (MSWD = 1.3; n = 13; Fig. 7b). Among these data, nine yield a concordia age of 290.6 ± 3.4 Ma ($MSWD_{(C+E)}$ = 1.3; n = 9). Both dates are similar; the best date estimate probably is the concordia age.

Among the sixteen-monazite crystals analysed in the deformed zone, nine are included in sillimanite aggregates and are anhedral, elongated and marking the foliation with patchy zonings (Fig. 6f). Two crystals (Mn 3 and 8) are included in biotite and show sub-euhedral shapes. Five monazite grains (Mn 9, 15, 32, 34 and 35) are in contact with both biotite and sillimanite. They are anhedral, stubbier with irregular borders and do not show a preferential orientation (Fig. 6e; Table S2). The spot analyses carried on the monazite crystals included in sillimanite and in biotite yield two similar concordia ages within error of 289 ± 2 Ma ($MSWD_{(C+E)}$ = 1.17; n = 13) and 297 ± 9 Ma ($MSWD_{(C+E)}$ = 2.6; n = 3), respectively (Fig. 7c). Combining all the analyses (except two) performed on the sixteen-monazite grains in the deformed zone yields a concordia age of 289.7 ± 2.0 Ma ($MSWD_{(C+E)}$ = 1.5; n = 14).

No correlation is observed within error between the textural position of the various populations (e.g. inclusion vs. matrix), U-Th-Pb contents and dates. Moreover, whatever the textural position of monazite, all dates are similar within uncertainties. Therefore, crystallization of monazite is unrelated to structural location and a single age can be calculated for the whole population. Thirty-one analyses on thirty monazite grains (inclusion and matrix) form a cluster, which yields a concordia age of 290.2 ± 1.6 Ma ($MSWD_{(C+E)}$ = 1.5; n = 31) (Fig. 7d).

**Samples from the C2 Shear Zones**

The Caladroy Shear Zone (CSZ) is the main C2 high strain zone that separates the supra and infrastructure (Fig. 8), and largely accommodated late-D2 thinning (Bouhallier, 1991; Vanardois et al., 2020; Siron et al., 2020). It appears as a kilometer-thick anastomosed network of mylonitic shear zones (C2) separating lens-shaped lower D2 strain domains where S2 predominates (Fig. 8a, Vanardois et al., 2020). Two meters-thick pegmatitic dykes were sampled in the core of the CSZ, located in the Brosse ravine (Fig. 8b). The pegmatite sample Ag03 is weakly deformed and lies within a low D2 strain domain, whereas sample Ag38 is strongly deformed and located in the core of a C2 shear zone.

*The Brosse ravine weakly deformed pegmatite (Ag03)*

Sample Ag03 corresponds to a meter-thick dyke that is subconcordant to the S2 foliation within the sillimanite-bearing micaschists (Fig. 8c). The pegmatite contains xenoliths of the surrounding micaschists. The pegmatite consists of a coarse-grained Qtz + Kfs + Pl + Ms + Bt + Tur pegmatitic assemblage, with no clear preferential orientation of minerals, but with a weak solid-state deformation, attested by the recrystallization of quartz grains. Biotite is not chloritized and feldspar is slightly sericitized, indicating limited fluid-rock interaction.

Monazite crystals are anhedral, sometimes rounded or in a fragmented form, green and transparent to slightly opaque. BSE imaging shows some grains to have a weakly patching zonation (Fig. S1). Twenty-six analyses on twenty-three crystals were analysed (Table S2). These data show wide ranges with high to very high Pb (5443-13712 ppm), Th (46617-269584 ppm) and U (29933-105937 ppm) contents and moderate Th/U ratios (0.58-9.01; most 0.58-4.13). In the concordia diagram, all these data are concordant between 310 and 270 Ma (Fig. 9a). Two data are younger (dotted ellipses) than the rest, presumably because of minor radiogenic Pb loss. Omitting those two data and an older one yields a concordia age of 290.6 ± 1.6 Ma ($MSWD_{(C+E)}$ = 1.5; n = 23; Fig. 9a).

Zircon is euhedral, prismatic with a shape ratio up to 3:1 and usually metamict and brownish except two crystals, which are transparent and colourless. CL imaging shows that the two colourless zircons have concentric zoning, but for others no zonation could be observed due to the metamictization (Fig. S2). Twenty-five analyses were carried out on twenty zircons of which nineteen yield a lower intercept date of 305.2 ± 2.1 Ma (MSWD = 0.38) and among these data, eleven give a concordia age of 304.4 ± 2.6 Ma ($MSWD_{(C+E)}$ = 1.03) (Table S3; Fig. 9b). Except for datum Z9c, the concordant data are characterized by high Pb (102-330 ppm) and U (2425-7356 ppm, most 2425-3568 ppm) contents and low Th (4-13 ppm) concentrations (Table S3). The four discordant data slightly above the concordia curve have a similar range in Pb (113-174 ppm) and U (2532-3838 ppm) contents and higher Th contents (10-132 ppm) than those from the concordant data. All these data have very low Th/U (0.001-0.019; most of them are between 0.001-0.004). Moreover, the core analyses of Zr2, Zr4 and Zr15 are concordant at 1762 ±22 Ma, 501 ± 15 Ma and 359 ± 10 Ma, respectively (Table S3; Fig. 9b).

*The Brosse ravine mylonitic pegmatite (Ag38)*

The mylonitic pegmatite (Ag38) is located in a high-strain D2 along a decametric thick C2 shear zone (Fig. 8b). It shows the same mineralogical assemblage as Ag03 with Qtz + Kfs + Pl + Ms + Tur ± Grt. Feldspar is slightly sericitized. The pegmatite is strongly deformed and totally transposed along the C2 shearing plane. Quartz, feldspar, and tourmaline are strongly elongated and stretched along the N20 L2 stretching lineation trend (Fig. 8d).

Two types of monazite crystals can be distinguished macroscopically, according to their colour, either green and transparent (Mn 1 to 7) or yellow to greenish and slightly opaque (Mn 8 to 17). In both cases, they are anhedral, and have no zonation in BSE. Moreover, they have similar concentrations (U = 22009 – 101992 ppm (most > 50000 ppm); Th = 42249 – 92063 ppm; U/Th = 0,45 – 2,97) (Table S2). In the concordia diagram, the two populations of monazite cannot be distinguished (Fig. 9c). Twenty-six analyses on seventeen monazites were performed (S2 and Table S2). Except two data (Mn12 and Mn

8-1, dotted ellipses), all ellipses are concordant between 250 and 310 Ma and, excluding 5 analyses (dotted ellipse), yield a concordia age of 291.5 ± 1.6 Ma ($MSWD_{(C+E)}$ = 0.53; n = 19) (Fig. 9c).

Zircon crystals are euhedral, brown, usually metamict. In CL, they are uniform enough without real internal structures (Fig. S2). Twenty-four analyses were performed on twenty-two zircons (Table S3). Except data Z4 and Z34, all data have very low Th/U ratios (<< 0.1, most <0.001) with low Th contents (< 10 ppm). In the Tera-Wasserburg diagram, except two data (Zr6c and Zr29C around 310 Ma), all ellipses have a concordant to sub concordant position at ca. 300 Ma and are aligned along a common-Pb discordia (Fig. 9d). Amongst these twenty-two data, thirteen give a concordia age of 297.6 ± 2.3 Ma ($MSWD_{(C+E)}$ = 1.4; Fig. 9d).

*The Planèzes mylonitic pegmatite (Ag47)*

Sample Ag47 is a 10-meter thick mylonitized pegmatite in the micaschists of the suprastructure, north of the Planèzes village (Fig. 2**.** This pegmatite is mineralogically similar to the Brosse Ravine pegmatites and consists of Kfs + Qtz + Pl + Ms + Tur assemblage, with slightly sericitized feldspars. The pegmatite shows a strong D2 mylonitization and is transposed along a C2 shear zone. The C2 high-strain planar fabric and L2 lineation marked by elongated quartz and tourmaline crystals are steepened due to Late-D3 deformation (Fig. 3).

Only a few zircons could be analysed that are usually anhedral, metamict and brownish-pink coloured. Most crystals preserve at least some crystal faces, although on some others those faces are almost entirely erased. One crystal (Z1) is subhedral, transparent and colourless. Fifteen analyses on seven zircons were performed (Table S3). In the Tera-Wasserburg diagram, all data are concordant or sub-concordant and form two clusters at ~ 490-530 Ma (group 1) and ~ 300-330 Ma (group 2) (Table S3; Fig. 10). The three analyses of group 1 were acquired on a single atypical and colourless crystal (Zr1). The Pb, Th and U contents are between 34-95 ppm, 39-69 ppm and 431-1212 ppm, respectively and with low Th/U ratios < 0.1 (i.e 0.045-0.091). Two analyses (Zr1-1 and Zr1-2) yield a concordia age of 527.1± 9.4 Ma ($MSWD_{(C+E)}$ = 1.5; n = 2) and the third datum (Zr1-3) gives a younger date at 490 ± 12 Ma. The group 2 data were obtained from 12 analyses on 6 zircon crystals showing a very low Th content (<3 ppm), a high to very high U content (1453-3900 ppm) with a very low Th/U (<<0.01) (Table S3; Fig. 10). Ten ellipses give a lower intercept date at 299.5 ± 2.6 Ma (MSWD = 0.32) and among these data, nine yield a concordia age of 299.7 ± 2.7 ($MSWD_{(C+E)}$ = 0.56). Two concordant ellipses (Zr5-2 and Zr7-2) yield an older concordia age of 326.6 ± 6.2 Ma ($MSWD_{(C+E)}$ = 2.6; n = 2) (Table S3; Fig. 10).

**Samples from the Proto-D3 Tournefort area**

*The Tournefort pegmatitic dyke (Ag08)*

Sample Ag08 is a 30-centimeter thick pegmatitic dyke that intrudes the Tournefort diorite (Fig. 11a and b). It cross-cuts the magmatic S3 foliation of the Tournefort diorite in a place where S3 is NE-SW trending and interpreted by Vanardois et al. (2020) as Proto-D3 planar fabrics (Fig. 11b). The pegmatite consists of a Qtz + Kfs + Pl ± Ms assemblage and shows brittle structures and localized ductile deformation of quartz (Fig. 11c). The feldspars are unaltered.

Monazite is anhedral, rounded with few preserved faces, clear and light-yellow coloured. BSE images show that in some crystals, margins are irregular and there are cavities in rims where monazite might have been partly dissolved out. Moreover, some crystals contain mineral inclusions, are fractured and have a weak intergrowth zoning (Fig. S1). Fifteen analyses were carried out on ten monazite crystals characterized by a wide range of Pb (most 1603-5982 ppm), Th (most 81772-190088 ppm) and U (most 2084-15431 ppm) contents and Th/U ratios (most 7.1-26.7) (Table S2; Fig. 12a). Except for three analyses (2 discordant and 1 concordant), all these data yield a concordia age of 296.4 ± 2.4 Ma ($MSWD_{(C+E)}$ = 1.3; n = 13). The difference in date of ~45 Ma between the younger concordant date (Mn 13) (not plotted because partially outside the range) at 249 ± 9 Ma and the average date of the cluster may be the result of radiogenic Pb loss (Table S2; Fig. 12a).

Two zircon types were found in this sample. The first type consists of euhedral, clear, colourless zircon crystals with CL images showing concentric zoning and few inherited cores. The second type is defined by euhedral, metamict, opaque and red crystals and CL images exhibiting mainly grains with cores containing many inclusions and cavities and which are sometimes enveloped by thin and homogenous rims (Fig. S2). Twenty-seven analyses on both cores and rims of eighteen zircon grains were analysed (Table S3). In the Tera-Wasserburg diagram, three inherited cores are concordant at 621 ± 22 Ma, 432 ± 16 Ma and 390 ± 15 Ma (Fig. 12b). They have similar Pb, Th and U concentrations, of about 23-32 ppm, 83-112 ppm and 207-538 ppm respectively. Their Th/U ratios are 0.16, 0.22 and 0.54 (Table S3). However, the majority of the data are clustered between ca. 350 Ma and 290 Ma (Fig. 12b). In the single-analysis concordia ages histogram, the data are distributed into 2 main populations at ~295 Ma and at 320-330 Ma, with an additional data at 353 ±13 Ma (Fig. 12b; Table S3). The youngest population at 295 Ma is performed on eleven zircon rims from 6 colourless and 5 metamict zircon grains. The six colourless zircons yield concordant data and are characterized by moderate Pb (59-110 ppm) and Th (85-352 ppm) contents and high to very high U (1350-2455 ppm) and with low Th/U ratios (0.06-0.25; most 0.06-0.12). While the rims of five metamict zircon give four discordant data which are characterized by higher Pb (123-225 ppm) and U (2901-5254 ppm) contents and lower Th concentrations (31-82 ppm) and with Th/U at 0.01-0.02 (Table S3). The linear regression on all these data yields a date of 293.8 ± 3.4 Ma by lower intercept (MSWD = 0.16; n = 11). Among these data, nine give a concordia age of 295.5 ± 3.8 Ma ($MSWD_{(C+E)}$ = 1.9) (Fig. 12b). The best date estimate is probably the concordia age. The second population at 320-330 Ma consists of twelve concordant data performed on 10 colourless crystals (8 cores and 4 rims). These data have low to moderate in Pb (10-81 ppm) and in Th (36-168 ppm) and moderate to high U (199-1695 ppm most 199-465 ppm) contents and moderate Th/U ratios (0.1-0.42 most 0.14-0.42) (Table S3). The highest U contents (1131 and 1695 ppm) associated with the lowest Th/U ratios (0.01) are obtained on the rims of two zircon grains (Z15 and Z23). These twelve data yield a concordia age of 323.3 ± 3.8 Ma ($MSWD_{(C+E)}$ = 0.7; n = 12) (Fig. 12b).

*The garnet-bearing leucogranite dyke (Ag06)*

Sample Ag06 was collected north of the Tournefort diorite and east of the Saint-Arnac granite (Fig. 11a). Interference between far field deformation and local deformation induced by pluton emplacement makes a complex strain pattern where D2, Proto-D3 and D4 planar fabrics are observed (Fig. 11a)

(Vanardois et al. 2020). The sample Ag06 consists of a 2-meter thick peraluminous leucogranite dyke. This dyke cross-cuts the Tournefort diorite magmatic foliation, the S2 foliation observed in surrounding partially melted micaschists and M2 isograd (Fig. 11a). Field relationships suggest that the emplacement of the leucogranite (Ag06) post-dates M2 metamorphic peak, the emplacement of the Tournefort diorite and the Proto-D3 deformation. This interpretation is consistent with the lack of solid-state deformation of the magmatic assemblages consisting of Kfs + Pl + Qtz + Grt + Ms (Fig. 11c; Vanardois et al. 2020).

Most monazite crystals are subhedral but a few grains are slightly rounded and transparent, all are clear to pale yellow. BSE imaging shows that most grains present a weak concentric or intergrowth zoning (Fig. S1). Twenty-six analyses on twenty monazite grains were performed (Table S2; Fig. 12c). They are characterized by high Pb (1578-4029 ppm) and U (506-9127 ppm) and very high Th (37498- 140262 ppm) concentrations giving a range of relatively high to very high Th/U ratios (6.2-138; most 26.2-138) (Table S2). Except for two analyses (Mn7, Mn19r, dotted ellipses)), all data are concordant to subconcordant around 290-310 Ma (Fig. 12c). Twenty-two data give a concordia age of 298.2 ± 2.7 Ma ($MSWD_{(C+E)}$ = 1.7; n = 22) (Fig. 12c).

Zircon crystals are relatively small (~100 μm), transparent, slightly pink to opaque pink-brown and mostly are euhedral prismatic crystal fragments. CL imaging shows strong evidence of concentric or oscillatory igneous growth zoning with no obvious cores (Fig. S2). Twenty-eight analyses were carried out on twenty-one zircon grains (Fig. S2; Table S3). These data are characterized by a wide range of Pb (37-195 ppm), Th (94-1134 ppm) and U (807-4076 ppm) concentrations and Th/U ratios (0.08-0.67, most 0.11-0.67) (Table S3). The distribution of all ellipses near 300 Ma in the Tera-Wasserburg diagram suggests that discordant analyses are probably affected by a common Pb contamination (Fig. 12d). The linear regression on the data set gives a date of 295.0 ± 2.9 Ma by lower intercept (MSWD = 0.10; n = 28) and the eleven data yield a concordia age of 298.3 ± 3.2 Ma ($MSWD_{(C+E)}$ = 1.4; n = 11) (Fig. 12d). Both dates are equal within the uncertainties and the best date estimation is the concordia age.

**Samples from the Late-D3 Tournefort Deformation Zone**

*The Vivier orthogneiss (Ag48)*

The Vivier orthogneiss (Ag48) is a 200-meter-thick laccolith containing paragneiss and marble elongated xenoliths. It is located inside the D3 corridor at its westernmost edge (Fig. 3). It is composed of a Qtz + Kfs + Grt + Bt ± Pl assemblage. It is partially molten and deformed at high temperatures with myrmekites having replaced the margins of Kfs, and recrystallization of quartz and feldspars. The main fabric observed, which is vertical, is interpreted as a late-D3 foliation. The partial melting affecting the Vivier orthogneiss sample (Ag48) is pre-D3.

Monazite crystals are subhedral to anhedral, light yellow and transparent. BSE images show that most crystals present a patchy zoning occasionally surrounded by a rim (Fig. S1). The analysed crystals have Pb (2076-5805 ppm), Th (63234-195033 ppm) and U (3391-8618 ppm) contents and Th/U ratios (9.18-31.17), which vary from crystal to crystal and within the same monazite (Table S2). Twenty-eight spot analyses on eighteen monazite crystals were performed (Table S2; Fig. 13a). In the concordia diagram, all ellipses yield a concordia age of 299.7 ± 1.7 Ma ($MSWD_{(C+E)}$ = 1.4; n = 28) without apparent difference between the rims and cores of the various crystals.

Zircon crystals are euhedral, transparent and colourless to slightly pinkish. CL images also show complex internal textures such as the presence of inherited cores and concentric oscillatory zoning and patchy zoning textures (Fig. S2). Thirty-six analyses were carried out on twenty zircon grains (Table S3; Fig. 13b). Among these data, thirty-three are concordant between ca. 630 Ma and 290 Ma. In the single-analysis concordia ages histogram, the data are distributed into 4 variable-sized populations: two minor ones at 430-490 Ma (group 1) and 570-630 Ma (group 2) and two major groups at 510-570 Ma (group 3) and 300-350 Ma (group 4) and (Fig. 13b).

Group 1 dates are determined from 4 rims and 1 core that have moderate Pb (23-103 ppm) and Th (21-58 ppm) contents and low Th/U ratios (0.03-0.18). These five data are ranging from 446 ± 12 Ma to 479 ± 12 Ma and yield a weighted average of 462 ± 17 Ma (MSWD = 5.2) (Fig. 13b; Table S3).

Group 2 dates are acquired on four zircon cores, which are characterized by moderate Pb contents (11-74 ppm) and variable Th (26-300 ppm) and U (113-713 ppm) concentrations, with Th/U ratios ranging from 0.08-0.42. They yield a concordia age of 597.2 ± 7.7 Ma ($MSWD_{(C+E)}$ = 0.68) (Fig. 13b; Table S3).

Group 3 dates are obtained from 10 cores and 3 rims. Pb and Th contents ranging from 11-158 ppm and 20-148 ppm, respectively, characterize these data. The U contents of the rims (758-2088 ppm) are higher than those of the cores (131-645 ppm). Th/U ratios of the cores (0.06-0.6; most 0.06-0.25) are thus higher than those of the rims (0.05-0.03). These data give a weighted average of 541 ± 11 Ma (MSWD = 6.6; n = 13). Among these 13 dates, nine yield a concordia age of 551.8 ± 4.8 Ma ($MSWD_{(C+E)}$ = 1.1; n = 9) (Fig. 13b, Table S3).

Group 4 dates were determined from rims of ten zircon crystals characterized by moderate Th and Pb contents ranging from 5 to 18 ppm and 20 to 31 ppm, respectively, and by very low Th/U ratios from 0.01 to 0.03 (Table S3). Seven of these zircon rims yield a concordia age of 303.9 ± 5.5 Ma ($MSWD_{(C+E)}$ = 2.5). The rims of three zircon grains Zr31, Zr18 and Zr27 have older dates at 344 ± 9 Ma, 323 ± 9 Ma and 391 ± 11 Ma, respectively. These dates are probably meaningless because they correspond to a mixture between an old core (~ 550 Ma) and a younger rim (probably ~ 300 Ma) (Fig. 13b, Table S3).

*Latour de France leucogranite (Ag51)*

The Latour-de-France leucogranite (Ag51) is located to the southwest of Latour de France village, in the infrastructure (Fig. 2 and 3). It is a 50-meter thick pluton composed of Qtz + Kfs + Pl + Bt + Grt + Ms. It shows no visible solid-state deformation but microstructures such as myrmekites replacing Kfs margins, plastic deformation of quartz indicated by chessboard extinction and microfractures in Kfs infilled by quartz indicate that the leucogranite was deformed under sub-magmatic conditions (Fig. 14a). The pluton cross-cuts S2 foliations and C2 shear zones and was emplaced in a kilometre-scale D3 fold hinge (Fig. 3; Vanardois et al. 2020). These observations suggest that the Latour de France leucogranite sample (Ag51) is syn-late-D3.

Monazite is sub-euhedral prismatic with a shape ratio up to 2:1, transparent and light-yellow coloured. BSE images of most crystals show that the centre with a patchy zoning while rims are characterized by a darker, slight concentric zoning (Fig. S1). The analysed spots have high Pb (2611-4672 ppm), high to very high U (5958 – 14794 ppm) and very high Th (75731 – 147318 ppm) concentrations with a range of relatively moderate Th/U (6.3 - 16.6) (Table S2). Twelve analyses were performed on 10 crystals (Fig. 14b; Table S2). These twelve data yield a concordia age of 291.0 ± 2.0 Ma ($MSWD_{(C+E)}$ = 0.27; n = 12) (Fig. 14b).

Most of the zircon crystals analysed are euhedral, either prismatic with a shape ratio up to 3:1 or stubbier with a shape ratio of 1:1. They are transparent, slightly pink to opaque pink-brown. CL imaging shows strong evidence of concentric or oscillatory igneous growth zoning and the presence of some inherited cores (Fig. S2). Twenty-two analyses were carried out on nineteen zircon grains (Fig. 14c; Table S3). Among these analyses, eighteen have a concordant to discordant position around 290 Ma suggesting a common Pb contamination. The linear regression calculated with these 18 data yields a date of 288.4 ± 3.3 Ma by lower intercept (MSWD = 0.36; n = 18) and amongst nine data give a similar concordia age of 289.4 ± 4.2 Ma ($MSWD_{(C+E)}$ = 1.6; n = 9) (Fig. 14c). These data are obtained on rims and cores of crystal and present Th/U ratios ranging between 0.004 and 0.26 (most are between 0.004-0.06) (Table S3). Moreover, the analyses of two zircon cores (Zr12c, Zr24c) yield a concordia age of 549 ± 11 Ma ($MSWD_{(C+E)}$ = 1.7). Furthermore, a third analytical point (Zr36c) is concordant at 684 ± 23 Ma (Table S3; Fig. 14c). The Th/U ratios of these three data are between 0.43 and 0.17.

## Interpretation and discussion

### Pre-Variscan history: Cadomian and Ordovician magmatism

Two samples collected in the infrastructure, near Le Vivier (Ag48, Ag57), show an early and complex history with inherited Precambrian and Ordovician zircon population ages (Table 1; Fig. 5b and 13b). The single-analysis concordia ages histograms of the Vivier deformed leucogranite (Ag57) and the Vivier orthogneiss (Ag48) highlight the presence of two major date populations at 630-710 Ma and at 550-610 Ma and three variable-sized populations with a main one at 510-570 Ma and two minor ones at 430-490 Ma and 570-630 Ma (Fig. 12b) respectively. These Neoproterozoic and Cambrian zircon populations could be correlated with zircon crystallization events related to the development of the Pan-African (750-600 Ma) and Cadomian (590-540 Ma) orogens (Linnemann et al. 2014) (Fig. 5b). Moreover, the presence of the Ordovician zircon population in the Ag48 sample, that are essentially zircon rims, is also an evidence for an Ordovician tectono-thermal event, which is possibly related to the emplacement of the magmatic protolith of the Rivérole orthogneiss at 461 ± 3 Ma in the infrastructure of the Agly massif (Paquette et al. 2021). The concordia age obtained on the Vivier orthogneiss (Ag48) at 551.8 ± 4.8 Ma is interpreted as the magmatic protolith emplacement age, and indeed, it is consistent with the ages at ca. 540-530 Ma obtained on five igneous rocks from the Agly massif infrastructure by Tournaire Guille et al. (2019). Similar Ordovician and Cambrian magmatism is widely documented in the Pyrenees (Deloule et al. 2002; Castinieras et al. 2008; Casas et al. 2010, 2015; Liesa et al. 2011; Martinez et al. 2011; Lemirre 2016; Marti et al., 2019) and in the French Central massif (Pin and Lancelot 1982; Roger et al. 2004; Alexandre 2007; Lotout et al. 2017) and inherited Pan-African and Cadomian zircons are also common in the various massifs from the southwestern segment of the Variscan belt (e.g. Melleton et al. 2010; Denèle et al., 2014; Schnapperelle et al. 2020; Margalef et al., 2016; Roger et al. 2015, 2020). Their occurrence are related to a possible source region of the northeastern Gondwana margin (von Raumer et al. 2015; Linnemann et al. 2014; Couzinié et al. 2014; Chelle-Michou et al. 2017; Stephan et al. 2019).

**Middle Carboniferous crustal partial melting and magmatism event (ca. 340-320 Ma)**

Three zircon rims from the Vivier leucogranite (Ag57) and two inherited cores of slightly metamict zircon from the Planèzes mylonitic pegmatite (Ag47) yielded concordia ages of 339.5 ± 13 Ma and of 326.6 ± 6.2 Ma, respectively (Fig. 5b, 10b). The Tournefort undeformed pegmatite (Ag08) has a zircon population (cores and rims) that yielded a concordia age of 323.3 ± 3.8 Ma (Fig. 12b). These three dates are similar within error and define a 340-320 Ma event. Similarly, monazite and zircon ages of 340-320 Ma have been reported in migmatites from the southern French Central Massif (Faure et al. 2014), in migmatites and granites of the PAZ (Mezger and Gerdes 2016; Lopez-Sanchez et al., 2019; Schnapperelle et al. 2020) and migmatites of the NPZ (Lemirre 2016). However, the origin of this

Visean/Serpukhovian magmatic and metamorphic event in the foreland is still debated (Roger et al. 2015; Schnapperelle et al. 2020; Cugerone et al. 2021). Thermobarometric estimates on the Montagne Noire (MN) gneiss dome suggest that, between 330 and 320 Ma, the continental crust was slightly overthickened with a partially molten lower-middle crust, at a depth between 30 and 40 km (Trap et al. 2017; Whitney et al. 2020). In the Agly massif, this early event is only identified through inherited zircon populations. Although we are not enable to constrain the relationships between this early thermal event and the strain fabrics, we propose that the ~340-320 Ma record could be attributed to the D1 or early-D2 deformations.

**Peak of magmatism at ca. 305 Ma**

Our results, as well as additional data from the literature, show that most of the Agly massif magmatic bodies range in crystallization age between 308 and 304 Ma (Olivier et al. 2004, 2008; Tournaire Guille et al. 2019) (Fig. 15). The zircon grains from the two Brosse Ravine pegmatites (Ag38, Ag03) show high U and Th contents and very low Th/U ratios (most <0.004) (Table S3). Although the low Th/U ratios (<<0.01) is commonly interpreted as the fingerprint of metamorphic crystallization, magmatic zircons with low Th/U ratios (<0.1) have also been reported in high-$SiO_2$ and/or peraluminous granitoids (Lopez-Sanchez et al., 2016). Thus, we interpret the zircon concordia age at 304.4 ± 2.6 Ma from the weakly deformed Ag03 pegmatite (Fig. 9b) as the emplacement age. A similar zircon concordia age at 305.8 ± 6.8 Ma (Fig. 5b) is given by the undeformed Vivier leucogranite (Ag57), emplaced as a sill into the flat-lying S2 foliation. The sills of Ansignan charnockite and Cassagnes granite have been dated to 307 ± 3 Ma and to 308 ± 3 Ma (Tournaire Guille et al. 2019). They are intrusive into the migmatitic S2 foliation with concordant to slightly discordant cross-cutting relationships (Vanardois et al., 2020). This argues for the development of suprasolidus S2 foliation before 308 Ma. Several ID-TIMS analyses and one LA-ICPMS analysis on syn-S2 charnockitic sills yield emplacement ages at ca. 315 Ma (Fig. 15; Postaire 1982; Respaut and Lancelot 1983; Olivier et al. 2004; Tournaire Guille et al. 2019) that might bracket the oldest development of D2 deformation. The undeformed Vivier leucogranite (Ag57) also intrudes into the S2 and gives a zircon concordia age at 305.8 ± 6.8 Ma and a monazite concordia age at 299.7 ± 1.7 Ma (Fig. 5a). Both zircon and monazite dates are similar within uncertainties but it is more likely that the emplacement of the Vivier leucogranite is best constrained by the zircon concordia age at 305.8 ± 6.8 Ma. The 299.7 ± 1.7 Ma monazite age might represent a partial reset during late D2 fluid-rock interactions. Indeed, experimental, petrological and field studies (Roger et al. 2020 and references therein) have shown that fluid-assisted dissolution-precipitation mechanisms are effective in altering the chemical and isotopic composition of monazite, even at low temperatures (Hawkins and Bowring 1997; Townsend et al. 2000). These results are consistent with Siron et al. (2020) that dated M2 partial melting and S2 planar fabric at ca. 305 Ma within kinzigites from different structural levels of the infrastructure.

The U-Th-Pb ages of the syn-D3 Tournefort diorite and Saint-Arnac granite in the Tournefort Deformation zone (TDZ) between 308 and 304 Ma (Olivier et al. 2004, 2008) also constrain the timing of the Proto-D3 dextral strike-slip shearing (Fig. 15). We propose that the D3 deformation started with the development of a vertical S3 within the dextral Proto-D3 shear zone at ca. 308 Ma. Vertical planar fabrics are pathways for the ascent of melts from the lower crust towards the middle and upper crusts (e.g. de Saint-Blanquat et al. 1998; Handy et al. 2001). The southern part of the St-Arnac pluton and Tournefort diorite bear magmatic foliations parallel with the D3 foliation and the vertical migmatitic lineation suggests a vertical ascent of the magmas (Olivier et al. 2008; Vanardois et al. 2020). The northern part of the St-Arnac pluton is structured by gently dipping magmatic foliations and N050-trending lineation indicating a NE directed horizontal expansion that is consistent with the D3 dextral bulk kinematics during syn-tectonic pluton emplacement (Olivier et al. 2008).

**Late Carboniferous-early Permian metamorphism and deformation (ca. 300-295 Ma)**

Our U-Th-Pb result reports an age group between ca. 300 and 295 Ma. The age of 297.6 ± 2.3 Ma obtained on zircon of the mylonitic pegmatite (Ag38) is interpreted as the synkinematic emplacement of the pegmatite during D2 strain localization along C2 shear zones (Fig. 9d). Zircon rims and cores from the syn-C2 Planèzes mylonitic pegmatite (Ag47) located in the micaschists of the suprastructure yield a concordia age at 299.7 ± 2.7 Ma (Fig. 3 and 9). This date is consistent with the emplacement age of the Brosse Ravine pegmatite (Ag38) and can be interpreted as the syn-C2 emplacement age of the Planèzes pegmatite. Tournaire Guille et al. (2019) dated partial melting of a paragneiss at 299 ± 4 Ma and the crystallization of leucogranites in the infrastructure at 307 ± 3 and 298 ± 3 Ma (Fig. 15). The range of ages around 300 Ma are very consistent with the ages of ~296 to 300 Ma ages recently obtained on monazite overgrowths from mylonitized kinzigites (Siron et al. 2020) and might constrain the sub-solidus, solid-state, deformation during the onset of the cooling evolution of the Agly massif.

The undeformed garnet-bearing leucogranite dyke (Ag06) that crosscuts both the magmatic Proto-D3 foliation and the S2 foliation (Fig. 11a) yields zircon and monazite concordia ages at 298.3 ± 3.2 and 298.2 ± 2.7 Ma (Fig. 12c and d). Zircon rims and monazites from the undeformed Tournefort pegmatitic dyke (Ag08) yield similar concordia ages at 295.5 ± 3.8 Ma and 296.4 ± 2.4 Ma (Fig. 12a-b). These dates record the emplacement ages of the Ag06 and Ag08 dyke intrusions that crosscut the Proto-D3 foliation at ca 300-295 Ma. Finally, the Vivier orthogneiss sample (Ag48) is D3 deformed and yields concordia age on zircon and monazite at 303.9 ± 5.5 Ma and 299.7 ± 1.7 Ma, respectively (Table 1, Fig. 13). Both dates are similar within error bars. We interpret the monazite concordia age at ca. 300 Ma as the best age estimate of peak D3 deformation.

**Last-stage event at ca. 290 Ma**

Monazite from the Ag03 and Ag38 pegmatites gives concordia ages at 290.6 ± 1.6 Ma and 291.5 ± 1.6 Ma, respectively (Fig. 9a and b). Both pegmatites are located along a D2 high-strain zone (i.e. Caladroy Shear Zone) (Fig. 3a). There is no evidence of garnet- or biotite-breakdown reactions in these samples that could have induced monazite crystallization. Thus, we interpret these dates as the age the final stage of C2 strain localization in the Caladroy shear zone. It may correspond to the timing of deformation-recrystallization leading to a reset of the U-Th-Pb isotopic system via fluid-assisted, syn-kinematic, dissolution/precipitation monazite processes. The migmatitic paragneiss (Ag3B), from the upper structural levels of the infrastructure, shows a well-developed syn-partial melting S2 foliation that is also affected by localized millimeter-thick C2 shear zones. Irrespective of their textural position (e.g. included in garnet or in C2 high strain zones), all monazite dates give a concordia age at 290.2 ± 1.6 Ma (Fig. 7d). The lack of preservation of older ages in monazite included in peritectic phases like garnet, the numerous fractures in garnet, and the absence of garnet-consumption (Fig. 6) suggest that monazite were reset or re-crystallized during a penetrative fluid-rock interaction during the C2 shearing. In comparison with aforementioned ages, the C2 subsolidus shearing started at ca. 300 Ma and lasted until at least 290 Ma.

The event at 290 Ma is also recorded in Late-D3 structures. The Latour-de-France leucogranite (Ag51) emplaced in a F3 fold hinge along the southern edge of the D3 corridor (Fig. 3c). It has been dated by similar concordia ages obtained on zircon and monazite at 289.4 ± 4.2 Ma and 291 ± 2 Ma, respectively (Fig. 14). This date at ca. 290-291 Ma is interpreted as the emplacement age of the Latour-de-France leucogranite in the upper part of the infrastructure, contemporaneously with D3 folding (Fig. 3c). Crystallization of these magmatic bodies may have provided hydromagmatic fluids that could be partly responsible for the reset of monazite at ca. 290 Ma. In the Cap de Creus (PAZ), Van Lichterveld et al. (2017) documented a late post-solidus, hydrothermal remobilization at 290 Ma and coeval magmatism in a wrench tectonic regime (Carreras and Druguet 2014).

**Tectonic implications**

In the PAZ, flat-lying foliations with top-to-the-south kinematics have been described and interpreted as evidence of an early nappe stacking event (Denèle et al. 2009, 2014). These foliations were mostly transposed by pervasive dextral transpression (Gleizes et al. 1998a; Carreras and Druguet 2014) associated with a longitudinal extrusional crustal flow (Cochelin et al. 2017, 2021). A similar evolution is described in the Montagne Noire where a nappe stacking event (Charles et al. 2009; Faure et al. 2014) was followed by a pervasive dextral wrenching in a transtensional regime inducing a longitudinal flow of the partially molten crust between 315 and 300 Ma (Rabin et al. 2015; Roger et al. 2015; Trap et al. 2017). Some authors recently proposed that, prior to the longitudinal flow, a gravity-driven flow of the partially molten crust from the northward orogenic plateau towards its southern foreland occurred at ca. 320 Ma (Whitney et al. 2015; Roger et al. 2020; Vanderhaeghe et al. 2020). However, the pervasive deformation induced by the dextral wrenching in the PAZ and in the Montagne Noire prevents the full investigation of this hypothesis.

On the other hand, the Agly massif is fortunately only affected by local transcurrent tectonics, which allows to discuss the origin of the flat-lying foliation. Initially, this sub-horizontal foliation (S2) in the Agly massif was also interpreted as a southward nappe-stacking event (Bouhallier et al. 1991; Olivier et al. 2004). Nevertheless, Vanardois et al. (2020) recently emphasized the existence of a suprasolidus early planar fabric (S1) probably representing relics of crustal thickening, as well as the flat-lying S2 foliation coeval with the crustal thinning of the massif documented by Siron et al. (2020). Olivier et al. (2004) highlighted top-to-the-South kinematics of the supra-solidus S2 foliations whereas the CSZ located at the anatectic front displays top-to-the-North kinematics (Bouhallier et al. 1991; Vanardois et al. 2020). In addition, Siron et al. (2020) documented a crustal thinning of ca. 5 km induced by the CSZ. Considering the tow dip of the CSZ (ca. 10-20° northward), such crustal thinning necessitated a horizontal displacement of at least 15-30 km between the infra- and suprastructure. Therefore, we propose that the supra-solidus S2 foliation developed in response to a horizontal flow of the partially molten crust towards the South (Fig. 16a). Our U-Th-Pb results and compilation on the Agly massif highlight that the S2 foliation developed at least at ca. 315 Ma and very likely at ca. 325-320 Ma during the onset of partial melting (Fig. 15). HT metamorphism and migmatization between ca. 340–320 Ma has been already documented in the NPZ and PAZ (Lemirre 2016; Mezger and Gerdes 2016; Lopez-Sanchez et al., 2019; Schnapperelle et al. 2020), which might indicate that the whole Variscan Pyrenees have also been affected by this southward horizontal flow. In the French Massif Central, the high-temperature/medium-pressure metamorphism and the emplacement of syntectonic plutons from 345 to 310 Ma is interpreted as the record of a major Carboniferous thermal anomaly that was responsible for the building of the orogenic plateau by gravity-driven lateral flow of the partially molten orogenic root toward the south (Whitney et al. 2015; Vanderhaeghe et al. 2020; Pitra et al. 2021). A similar process of gravity-driven flow has also been proposed in other Variscan massifs (Schulmann et al. 2008, 2014; Diez Fernandez and Pereira 2016; Pereira et al. 2018). A channel flow progressing from the French Central Massif to the Pyrenees would necessitate synchronous extension setting in the hinterlands and compressional regime in the forelands (Rey et al., 2010; Whitney et al. 2013), but our results rather suggest coeval extension in both hinterlands and forelands between 325-310 Ma. Considering the presence of a Visean – Serpukhovian magmatism and metamorphism in the PAZ and NPZ (Mezger and

Gerdes 2016; Schnapperelle et al. 2020; Cugerone et al. 2021; this study), it seems likely that the lower crust of the Variscan Pyrenees was already in high-temperature conditions at 325-310 Ma and probably molten. Therefore, we propose that the whole lower crust of the PAZ, NPZ and Montagne Noire melted at ca. 325-310 Ma and flowed towards the South over short to moderate distances (Fig. 17a), rather than being implicated in a large-scale horizontal channel flow from the northern French Central Massif to the Pyrenees..

The syn-tectonic emplacements of the Tournefort diorite and St-Arnac granite in the TDZ (Vanardois et al. 2020) indicate that the dextral wrenching started at ca. 308 Ma in the Agly massif, acting as pathways for melt, enhancing the emplacement of plutons in the upper crust (Fig. 16b and c). Similar emplacement of plutons driven by vertical dextral shear zones at 310-300 Ma are widely described in the PAZ (e.g. Gleizes et al. 1998b, 2001, 2006; Aujérac et al. 2004; Román-Berdiel et al. 2006; Antolín-Tomás et al. 2009) or in the Montagne Noire (Trap et al. 2017; Roger et al. 2020), synchronously with the longitudinal flow of the lower crust (Cochelin et al. 2017, 2021; Trap et al. 2017; Roger et al. 2020). The limited dextral deformation in the Agly massif and in the other areas of the NPZ compared to the PAZ and the Montagne Noire is interpreted as a strain gradient across a lithospheric-scale ductile dextral wrench zone represented by the PAZ (Fig. 17b). In the PAZ, during ongoing transpression, the high-strain dextral shearing reworked the flat-lying foliations related to gravity-driven flow into a longitudinal flow. On the contrary, in the Agly massif, the dextral wrenching remained limited within the partially molten crust, which was still recording southward flow until ca. 300 Ma (Fig. 16b and c, 17b). Rey et al. (2017) have demonstrated that local contractional structures can be produced by flow of the molten crust during extensional regime, which could correspond to the coeval D2 extensive and D3 compressive structures in the Agly massif.

These results highlight a high-temperature protracted event responsible for crustal partial melting for at least 15-20 Ma. The origin of the heat supply needed necessary to produce these high-temperature conditions in the southern part of the Variscan belt as well as the source of the mantle-derived magmas remain controversial. Several authors proposed deep thermal anomalies related to the delamination of the lithospheric mantle induced by a slab roll-back in the French Central Massif (e.g. Laurent et al.

2017; Vanderhaeghe et al. 2020) or affecting the whole Gondwana lithosphere (Lemirre et al., 2019), to mantellic plumes in the whole Variscan belt (Franke 2014, 2017), to ridge subduction and slab window formation in the massifs of southwestern Iberia (Rodriguez et al. 2022; Pereira et al. 2022) or to a sub-lithospheric or intra-crustal relamination and magmatic flow as recently proposed in the Bohemian massif (Maierova et al. 2018, 2021).

After the crystallization of most of the anatectic melts in the infrastructure of the Agly massif, the dextral wrenching lasted until 290 Ma in the TDZ (Fig. 15). Our results also highlight that C2 subsolidus flat-lying shear zones were still active at ca. 290 Ma (Fig. 15) with top-to-the-North kinematics (Vanardois et al. 2020). We propose that these shear zones accommodated local extensional regime in the D3 dextral low-strain domains within the NPZ (e.g. Denèle et al. 2014), while transpression was still active in the PAZ and in the Montagne Noire (Cochelin et al. 2017; Roger et al. 2020) (Fig. 17c). In the PAZ and NPZ, Permian magmatism and volcanism in basins has been emphasized by numerous geochronological studies (Denèle et al. 2012; Rodriguez-Mendez et al., 2014; Druguet et al. 2014; Pereira et al., 2014; Lemirre 2016; Kilzi et al., 2016; Van Lichtervelde et al. 2017; Lopez-Sanchez et al., 2018; Poitrenaud et al. 2020; this study). These Permian volcanic and plutonic rocks highlight that the Pyrenean crust was still in anomalous high thermal conditions at the end of the Variscan orogeny. The origin of these Permian high-thermal conditions may be related to a combination of the Paleotethys subduction and an extensive-transtensive setting (e.g. Debon and Zimmermann, 1993; Lago et al., 2004; Gil-Imaz et al., 2012; Pereira et al., 2014).

## Conclusion

Our geochronological results and the compilation of available ages on the Agly massif indicate that the Variscan lower-middle crust was partially molten from ca. 325 to 300 Ma. These new results emphasize the first evidence of middle Carboniferous event at ca. 325 Ma in the Agly massif. We also highlight a partitioning of the deformation between flat-lying foliations D2 and a dextral shear zone D3 from ca. 308 Ma to 290 Ma. The compilation of geochronological data on the Agly massif and a comparison with tectonic evolutions known for the Montagne Noire and of the Pyrenean Axial Zone allow us to propose a tectonic evolution for the southern edge of the French Central Massif: (i) the maturation of the orogenic crust induced the widespread partial melting of the lower-middle crust in hinterlands and forelands. This was responsible for a horizontal flow from the French Central Massif to the PAZ towards the South at ca. 325 Ma. (ii) Dextral wrenching affecting the whole Variscan belt became pervasive in the Montagne Noire and in the PAZ and reoriented the southward flow into an E-W longitudinal flow, while the NPZ was only locally affected by this dextral wrenching that did not reorient the southward flow. (iii) The crystallisation of most of the anatectic melts stopped the flow of the lower crust at ca. 300 Ma. The dextral wrenching remained active until 290 Ma in the Agly massif, the PAZ and the MN. Synchronously with the local wrenching in the TDZ of the Agly massif, subsolidus C2 shear zones accommodated a local extensional regime in the NPZ until ca. 290 Ma.

## Acknowledgments

We dedicate this article to Jean-Louis Paquette who sadly passed away in June. This research was supported by the BRGM through the Référentiel Géologique de la France program (RGF program). We thank Cyprien Astoury for mineral separation. Didier Convert provided generous support with thin section preparation. We thank the MIMENTO technology center for the SEM provision.

## Declarations

Conflict of interest: The authors declare that they have no known competing financial interests or personal relationships that could have appeared to influence the work reported in this paper.

## References

Aguilar C, Liesa M, Castiñeiras P, Navidad M (2013) Late Variscan metamorphic and magmatic evolution in the eastern Pyrenees revealed by U–Pb age zircon dating. J Geol Soc London 171:181-192.

Alexandre P (2007) U–Pb zircon SIMS ages from the French Massif Central and implication for the pre-Variscan tectonic evolution in Western Europe. C R Geosc, 339:613-621.

Althoff F, Barbey P, Pons J (1994) La charnockite d'Ansignan et le granite de Saint-Arnac, témoins d'une extension crustale d'âge hercynien dans le massif de l'Agly (Pyrénées Orientales, France). CR Acad Sci Paris 319:239-246.

Andrieux P (1982a) Conditions de cristallisation et évolution paragénétique d'une charnockite hercynienne: le complexe granulitique d'Ansignan (massif de l'Agly, Pyrénées-Orientales). B Minéral 105:253–266.

Andrieux P (1982b) La charnockite d'Ansignan (Massif d'Agly, Pyrénées Orientales). Mise en place et évolution paragénétique. Introduction à l'étude des équilibres grenat – orthopyroxène. 3rd Cycle Thesis, Clermont-Ferrand (France): Univ. Blaise Pascal.

Antolín-Tomás B, Román-Berdiel T, Casas-Sainz A, Gil-Peña I, Oliva B, Soto R (2009) Structural and magnetic fabric study of the Marimanha granite (Axial Zone of the Pyrenees). Int J Earth Sci 98: 427–441.

Auréjac JB, Gleizes G, Diot H, Bouchez JL (2004) Le complexe granitique de Quérigut (Pyrénées, France) ré-examiné par la technique de l'ASM: un pluton syntectonique de la transpression dextre hercynienne. Bull Soc geol Fr 175: 157–174.

Berger GM, Fonteilles M, Leblanc D, Clauzon G, Marchal JP, Vautrelle C (1993) Notice de la carte géologique de la France, feuille Rivesaltes (1090), scale 1:50 000. Orléans : BRGM.

Bouhallier H, Choukroune P, Ballevre M (1991) Evolution structurale de la croûte profonde hercynienne : exemple du massif de l'agly (Pyrenees-Orientales, France). CR Acad Sci Paris 312:647-654.

Carreras J, Druguet E (2014) Framing the tectonic regime of the NE Iberian Variscan segment. Geol Soc Spec Publ London 405. doi.org/10.1144/SP405.7

Casas JM, Castiñeiras P, Navidad M, Liesa M, Carreras J (2010) New insights into the Late Ordovician magmatism in the Eastern Pyrenees: U–Pb SHRIMP zircon data from the Canigó massif. Gondwana Res 17:317-324.

Casas JM, Navidad M, Castiñeiras P, Liesa M, Aguilar C, Carreras J, Hofmann M, Gärtner A, Linnemann U (2015) The Late Neoproterozoic magmatism in the Ediacaran series of the Eastern Pyrenees: new ages and isotope geochemistry. Int J Earth Sci 104:909-925.

Castiñeiras P, Navidad M, Liesa M, Carreras J, Casas JM (2008) U–Pb zircon ages (SHRIMP) for Cadomian and Early Ordovician magmatism in the Eastern Pyrenees: new insights into the pre-Variscan evolution of the northern Gondwana margin. Tectonophysics 461:228-239.

Chardon D, Aretz M, Roques D (2020) Reappraisal of Variscan tectonics in the southern French Massif Central. Tectonophysics 787, 228477.

Charles N, Faure M, Chen Y (2009) The Montagne Noire migmatitic dome emplacement (French Massif Central): new insights from petro-fabric and AMS studies. J Struct Geol 31, 1423–1440.

Chelle-Michou C, Laurent O, Moyen JF et al (2017) Pre-Cadomian to late-Variscan odyssey of the eastern Massif Central, France: Formation of the West European crust in a nutshell. Gondwana Res. 46:170-190.

Clark MK, Royden LH (2000) Topographic ooze: building theeastern margin of Tibet by lower crustal flow. Geology 28, 703–706.

Cochelin B, Chardon D, Denèle Y, Gumiaux C, Le Bayon B (2017) Vertical strain partitioning in hot Variscan crust: Syn-convergence escape of the Pyrenees in the Iberian-Armorican syntax. Bull Soc Geol Fr 188. https://doi.org/10.1051/bsgf/2017206

Cochelin B, Lemirre B, Denèle Y, de Saint Blanquat M (2021) Strain partitioning within bending orogens, new insights from the Variscan belt (Chiroulet-Lesponne domes, Pyrenees). Tectonics, 40, e2020TC006386. https://doi.org/10.1029/2020TC006386

Couzinié S, Moyen JF, Villaros A, Paquette JL, Scarrow JH, Marignac C (2014) Temporal relationships between Mg-K mafic magmatism and catastrophic melting of the Variscan crust in the southern part of Velay Complex (Massif Central, France). J Geosci 59:1-18.

Cugerone A, Roger F, Cenki-Tok B, Oliot E, Paquette JL (2021) Variscan U-Th-Pb age for stratabound Pb-Zn mineralization in the Bossòst dome (Pyrenean Axial Zone), Ore Geol Rev, 139: 104503. https://doi.org/10.1016/j.oregeorev.2021.104503

de Saint Blanquat M (1993) La faille normale ductile du massif de Saint-Barthélémy. Evolution hercynienne des massifs nord-pyrénéens catazonaux considérée du point de vue de leur histoire thermique. Geodin Acta 6:59-77.

de Saint Blanquat M, Tikoff B, Teyssier C, Vigneresse JL (1998) Transpressional kinematics and magmatic arcs. In: Holdsworth RE, Strachan RA, Dewey JF (Eds.), Continental Transpressional and Transtensional Tectonics. Geol Soc Spec Publ, 135:327–340.

Debon F, Zimmermann JL (1993) Mafic dykes from some plutons of the Western Pyrenean Axial Zone (France, Spain): markers of the transition from Late-Hercynian to early Alpine events. Schweizerische Mineralogische und Petrographische Mitteilungen 73:421–433.

Delay F (1989) Le massif nord-pyrénéen de l'Agly (Pyrénées orientales) : Évolution tectono-métamorphique et exemple d'un amincissement crustal polyphasé. PhD thesis, Lille (France): Univ. Lille 1.

Deloule E, Alexandrov P, Cheilletz A, Laumonier B, Barbey P (2002) In-situ U–Pb zircon ages for Early Ordovician magmatism in the eastern Pyrenees, France: the Canigou orthogneisses. International Journal of Earth Sciences 91:398-405.

Denèle Y, Olivier P, Gleizes G, Barbey P (2009) Decoupling between the Middle and Upper Crust during Transpression-Related Lateral Flow: Variscan Evolution of the Aston Gneiss Dome (Pyrenees, France). Tectonophysics 477: 244–261.

Denèle Y, Paquette JL, Olivier P, Barbey P (2012) Permian granites in the Pyrenees: the Aya pluton (Basque Country). Terra Nova 24:105-113.

Denèle Y, Laumonier L, Paquette JL, Olivier P, Gleizes G, Barbey P (2014) Timing of granite emplacement, crustal flow and gneiss dome formation in the Variscan segment of the Pyrenees. Geol Soc London Spec Publ 405:265-287.

Díez Fernández R, Pereira MF (2016) Extensional orogenic collapse captured by strike-slip tectonics: Constraints from structural geology and U-Pb geochronology of the Pinhel shear zone (Variscan orogen, Iberian Massif). Tectonophysics 691:290-310.

Druguet E (2001) Development of high thermal gradients by coeval transpression and magmatism during the Variscan orogeny: insights from the Cap de Creus (Eastern Pyrenees). Tectonophysics, 332:275-293.

Druguet E, Castro A, Chichorro M, Pereira MF, Fernández C (2014) Zircon geochronology of intrusive rocks from Cap de Creus, Eastern Pyrenees. Geol Mag, 151:1095-1114.

Dumond G, Goncalves P, Williams ML, Jercinovic MJ (2015) Monazite as a monitor of melting, garnet growth and feldspar recrystallization in continental lower crust. J Metamorph Geol 33:735-762.

Edel JB, Schulmann K, Lexa O, Lardeaux JM (2018) Late Palaeozoic palaeomagnetic and tectonic constraints for amalgamation of Pangea supercontinent in the European Variscan belt. Earth Sci Rev 177:589-612.

Faure M, Cocherie A, Gaché J et al. (2014) Middle Carboniferous intracontinental subduction in the Outer Zone of the Variscan Belt (Montagne Noire Axial Zone, French Massif Central): multi-method geochronological approach of polyphase metamorphism. In: Schulmann K, Martinez Catalan JR, Lardeaux JM, Janousek V, Oggiano G (Eds.), The Variscan Orogeny: Extent, Timescale and the Formation of the European Crust. Geol Soc London, Spec Publ 405. http://dx.doi.org/10.1144/SP405.2.

Fonteilles M, Guitard G, Raguin E (1964) Sur la présence de gneiss à disthène et cordiérite dans le massif du Saint-Barthélémy (Pyrénées de l'Ariège). CR Acad Sci Paris 258:3524–3525.

Fonteilles M (1970) Géologie des terrains métamorphiques et granitiques du massif hercynien de l'Agly (Pyrénées orientales). Bull BRGM 3:1-54.

Fonteilles M, Guitard G (1971) Disthène relique et disthène hystérogène dans les terrains métamorphiques hercyniens des Pyrénées orientales franco-espagnoles. CR Acad Sci Paris 272:361-363.

Fonteilles M, Leblanc D, Clauzon G, Vaudin JL, Berger GM (1993) Carte géologique de la France, feuille Rivesaltes (1090), scale 1:50 000. Orléans : BRGM.

Franke W (2014) Topography of the Variscan orogen in Europe: Failed—not collapsed: Int J Earth Sci, 103, 1471–1499, doi:10.1007/s00531-014-1014-9

Franke W (2017) The origin of contractional structures in extensional gneiss domes: COMMENT. Geology 45, e415. https://doi.org/10.1130/G39092C.1.

Franke W, Cocks LRM, Torsvik TH (2017) The Palaeozoic Variscan oceans revisited. Gondwana Res 48:257-284. https://doi.org/10.1016/j.gr.2017.03.005

Gerbault M, Martinod J, Herail G (2005) Possible orogeny-parallel lower crustal flow and thickening in the central Andes. Tectonophysics, 399:59–72, doi:10.1016/j.tecto.2004.12.015.

Gil-Imaz A, Lago-San José M, Galé C, Pueyo-Anchuela O, Ubide T, Tierz P, Oliva-Urcia B (2012) The Permian mafic dyke swarm of the Panticosa pluton (Pyrenean Axial Zone, Spain): simultaneous emplacement with the late-Variscan extension. Journal of Structural Geology 42:171–183.

Gleizes G, Leblanc D, Bouchez JL (1998a) The main phase of the Hercynian orogeny in the Pyrenees is a dextral transpression. Geol Soc London Spec Publ 135: 267–273.

Gleizes G, Leblanc D, Santana V, Olivier O, Bouchez JL (1998b) Sigmoidal structures featuring dextral shear during emplacement of the Hercynian granite complex of Cauterets–Panticosa (Pyrenees). J Struct Geol 20:1229–1245.

Gleizes G, Leblanc D, Olivier P, Bouchez JL (2001) Strain partitioning in a pluton during emplacement in transpressional regime: The Example of the Néouvielle Granite (Pyrenees). Int J Earth Sci 90: 325–340.

Gleizes G, Crevon G, Asrat A, Barbey P (2006) Structure, age and mode of emplacement of the Hercynian Bordères-Louron pluton (Central Pyrenees, France). Int J Earth Sci 95:1039–1052.

Goncalves P, Nicollet C, Montel JM (2004) Petrology and in situ U–Th–Pb monazite geochronology of ultrahigh-temperature metamorphism from the Andriamena mafic unit, north–central Madagascar. Significance of a petrographical P–T path in a polymetamorphic context. J Petrol, 45:1923-1957.

Handy MR, Mulch A, Rosenau M, Rosenberg CL (2001) The role of fault zone and melts as agents of weakening, hardening and differentiation of the continental crust: A synthesis, in: Holdsworth RE et al. (eds) Nature and Tectonic Significance of Fault Zone Weakening, Geol Soc London Spec Publ, 186, 305–332.

Hawkins DP, Bowring SA (1997). U-Pb systematics of monazite and xenotime: case studies from the Paleoproterozoic of the Grand Canyon, Arizona. Contrib Mineral Petrol 127:87-103

Hurai V, Paquette,JL, Huraiová M, Konečný P (2010) Age of deep crustal magmatic chambers in the intra-Carpathian back-arc basin inferred from LA-ICPMS U-Th-Pb dating of zircon and monazite from igneous xenoliths in alkali basalts. J Volc Geo Res 198:275-287.

Jaffey AH, Flynn KF, Glendenin LE, Bentley WC, Essling AM (1971) Precision measurement of half-lives and specific activities of 235U and 238U. Phys Rev C4, 1889–1906.

Kilzi MA, Grégoire M, Bosse V, Benoit M, Driouch Y, de Saint Blanquat M, Debat P (2016) Geochemistry and zircon U–Pb geochronology of the ultramafic and mafic rocks emplaced within the anatectic series of the Variscan Pyrenees: The example of the Gavarnie–Heas dome (France). C R Geosci, 348:107-115.

Lago M, Arranz E, Pocoví A, Galé C, Gil-Imaz A (2004) Permian magmatism and basin dynamics in the southern Pyrenees: a record of the transition from late Variscan transtension to early Alpine extension. In: Wilson M, Neumann ER, Davies GR, Timmerman MJ, Heeremans M, Larsen BT (Eds.), Permo-Carboniferous Magmatism and Rifting in Europe. Geol. Soc. Lond. Spec. Publ., 223, pp. 439–464 (London).

Laurent O, Couzinié S, Zeh A, Vanderhaeghe O, Moyen JF, Villaros A, Gardien V, Chelle-Michou C (2017) Protracted, coeval crust and mantle melting during Variscan late orogenic evolution: U–Pb dating in the eastern French Massif Central. Int J Earth Sci 106:421-451.

Lemirre B (2016). Origine et développement de la thermicité dans les Pyrénées varisques. PhD thesis, Toulouse (France), Univ. Toulouse.

Lemirre B, Cochelin B, Duchêne S, de Saint Blanquat M, Poujol M (2019) Origin and duration of late orogenic magmatism in the foreland of the Variscan belt (Lesponne—Chiroulet—Neouvielle area, french Pyrenees). Lithos 336:183-201.

Liesa M, Carreras J, Castiñeiras P, Casas JM, Navidad M, Vilà, M (2011) U-Pb zircon age of Ordovician magmatism in the Albera Massif (Eastern Pyrenees), Geol Acta 9:1–9.

Linnemann U, Ouzegane K, Drareni A, Hofmann M, Becker S, Gärtner A, Sagawe A (2011) Sands of West Gondwana: an archive of secular magmatism and plate interactions — a case study from the Cambro-

Ordovician section of the Tassili Ouan Ahaggar (Algerian Sahara) using U–Pb LA-ICP-MS detrital zircon ages. Lithos 123:188–203.

Linnemann U, Gerdes A, Hofmann M, Marko L (2014) The Cadomian Orogen: Neoproterozoic to Early Cambrian crustal growth and orogenic zoning along the periphery of the West African Craton — Constraints from U–Pb Zircon Ages and Hf isotopes (Schwarzburg Antiform, Germany). Precambrian Res 244:236–278.

Lopez-Sanchez MA, Aleinikoff JN, Marcos A, Martínez FJ, Llana-Fúnez S (2016) An example of low-Th/U zircon overgrowths of magmatic origin in a late orogenic Variscan intrusion: the San Ciprián massif (NW Spain). J Geol Soc 173:282–291.

Lopez-Sanchez MA, García-Sansegundo J, Martínez FJ (2019) The significance of early Permian and early Carboniferous U–Pb zircon ages in the Bossòst and Lys-Caillaouas granitoids (Pyrenean Axial Zone). Geol J 54:2048-2063.

Lotout C, Pitra P, Poujol M, Van Den Driessche J (2017) Ordovician magmatism in the Lévézou massif (French Massif Central): tectonic and geodynamic implications. Int J Earth Sci 106:501-515.

Ludwig KR (2001) User manual for Isoplot/Ex rev. 2.49. A geochronological toolkit for Microsoft Excel. Berkeley Geochronology Center Special Publication 1a, 1–56.

Maierová P, Schulmann K, Lexa O et al (2016) European Variscan orogenic evolution as an analogue of Tibetan-Himalayan orogen: Insights from petrology and numerical modeling. Tectonics 35:1760–1780.

Maierová P, Schulmann K, Gerya T (2018) Relamination styles in collisional orogens. Tectonics 224–250

Maierova P, Schulmann K, Stípska P, Gerya T, Lexa O (2021) Trans-litospheric diapirism explains the presence of ultra-high pressure rock in the European Variscides. Commun. Earth Environ. 2, 56. https://doi.org/10.1038/s43247-021-00122-w.

Margalef A, Castiñeiras P, Casas JM, Navidad M, Liesa M, Linnemann U, Hofmann M, Gärtner A (2016) Detrital zircons from the Ordovician rocks of the Pyrenees: Geochronological constraints and provenance. Tectonophysics 681:124-134.

Martí J, Solari L, Casas JM, Chichorro M (2019) New late Middle to early Late Ordovician U–Pb zircon ages of extension-related felsic volcanic rocks in the Eastern Pyrenees (NE Iberia): tectonic implications. Geol Mag, 156:1783-1792.

Martínez FJ, Iriondo A, Dietsch C, Aleinikoff JN, Peucat JJ, Cirès J, Reche J, Capdevila R (2011) U-Pb SHRIMP-RG zircon ages and Nd signature of lower Paleozoic rifting-related magmatism in the Variscan basement of the Eastern Pyrenees. Lithos, 127:10-23.

Martínez Catalán JR, Schulmann K, Ghienne JF (2021) The Mid-Variscan Allochthon: Keys from correlation, partial retrodeformation and plate-tectonic reconstruction to unlock the geometry of a non-cylindrical belt. Earth-Sci Rev 220:103700.

Melleton J, Cocherie A, Faure M, Rossi P (2010) Precambrian protoliths and Early Paleozoic magmatism in the French Massif Central: U–Pb data and the North Gondwana connection in the west European Variscan belt. Gondwana Res 17:13-25.

Mezger J, Gerdes A (2016) Early Variscan (Visean) granites in the core of central Pyrenean gneiss domes: implications from laser ablation U-Pb and Th-Pb studies. Gondwana Res 29:181-198.

Odlum ML, Stockli DF (2019) Thermotectonic evolution of the North Pyrenean Agly Massif during Early Cretaceous hyperextension using multi-mineral U-Pb thermochronometry. Tectonics, 38. doi.org/10.1029/2018TC005298

Olivier P, Gleizes G, Paquette JL (2004) Gneiss domes and granite emplacement in an obliquely convergent regime: new interpretation of the Variscan agly massif (eastern Pyrenees, France), Geol. Soc. Am. sp. pap. 380:229-240.

Olivier P, Gleizes G, Paquette JL Muñoz Sáez C (2008) Structure and U–Pb Dating of the Saint-Arnac Pluton and the Ansignan Charnockite (Agly Massif): A Cross-Section from the Upper to the Middle Crust of the Variscan Eastern Pyrenees. J Geol Soc 165:141 52.

Paquet J, Mansy JL (1991) The structure of the Eastern Pyrenees (transect of the Agly massif): an example of crustal thinning. CR Acad Sci Paris 312:913-919.

Paquette JL, Tiepolo M (2007) High resolution (5 µm) U-Th-Pb isotopes dating of monazite with excimer laser ablation (ELA)-ICPMS. Chem Geol, 240, 222-237.

Paquette JL, Piro, JL Devidal JL, Bosse V, Didier A (2014). Sensitivity enhancement in LA-ICP-MS by N2 addition to carrier gas: application to radiometric dating of U–Th-bearing minerals. Agilent ICP-MS J 58, 4–5.

Paquette JL, Barbey P, Olivier P (2021) Âge ordovicien moyen et caractéristiques chimiques du gneiss de la Rivérole (Massif de l'Agly, Pyrénées orientales). Bull Soc Hist nat Toulouse 156:111-119

Pereira MF, Castro A, Chichorro M, Fernández C, Diaz-Alvarado J, Martí J, Rodríguez C (2014) Chronological link between deep-seated processes in magma chambers and eruptions: Permo-Carboniferous magmatism in the core of Pangaea (Southern Pyrenees). Gondwana Res 25:290-308.

Pereira MF, Díez Fernández R, Gama C, Hofmann M, Gärtner A, Linnemann U (2018) S-type granite generation and emplacement during a regional switch from extensional to contractional deformation (Central Iberian Zone, Iberian autochthonous domain, Variscan Orogeny). Int J Earth Sci 107:251-267.

Pereira MF, Fuenlabrada JM, Rodríguez C, Castro A (2022) Changing Carboniferous Arc Magmatism in the Ossa-Morena Zone (Southwest Iberia): Implications for the Variscan Belt. Minerals 12:597.

Pin C, Lancelot J (1982) U-Pb dating of an early Paleozoic bimodal magmatism in the French Massif Central and of its further metamorphic evolution. Contrib Mineral Petrol 79:1-12.

Pitra P, Poujol M, Van Den Driessche J, Bretagne E, Lotout C, Cogné N (2021) Late Variscan (315 Ma) subduction or deceiving zircon REE patterns and U-Pb dates from migmatite-hosted eclogites? (Montagne Noire, France). J Metamorph Geol, in press. https://doi.org/10.1111/jmg.12609

Poitrenaud T, Poujol M, Augier R, Marcoux E (2020) The polyphase evolution of a late Variscan W/Au deposit (Salau, French Pyrenees): insights from REE and U/Pb LA-ICP-MS analyses. Mineral Deposita 55:1127-1147.

Postaire B (1982) Systématique Pb commun et U-Pb sur zircons: Applications aux roches de haut grade métamorphique impliquées dans la chaîne hercynienne (Europe de l'ouest) et aux granulites de Laponie (Finlande). Mémoires de la Société Géologique et Minéralogique de Bretagne 15:29–72.

Rabin M, Trap P, Carry N, Fréville K, Cenki-Tok B, Lobjoie C, Goncalves P, Marquer D (2015) Strain partitioning along the anatectic front in the Variscan Montagne Noire massif (Southern French Massif Central). Tectonics 34:1709–1735.

Respaut JP, Lancelot JR (1983) Datation de la mise en place synmétamorphe de la charnockite d'Ansignan (massif de l'Agly) par la méthode U/Pb sur zircons et monazites. Neues Jahrb Mineral Abh 147:21-34.

Rey PF, Teyssier C, Whitney DL (2010) Limit of channel flow in orogenic plateaux. Lithosphere, 2:328-332.

Rey PF, Teyssier C, Kruckenberg SC, Whitney DL (2011) Viscous collision in channel explains double domes in metamorphic core complexes. Geology 39:387-390.

Rey PF, Mondy L, Duclaux G, Teyssier C, Whitney DL, Bocher M, Prigent C (2017) The origin of contractional structures in extensional gneiss domes. Geology 45-263-266.

Rodríguez C, Pereira MF, Castro A, Gutiérrez-Alonso G, Fernández C (2022) Variscan intracrustal recycling by melting of Carboniferous arc-like igneous protoliths (Évora Massif, Iberian Variscan belt). GSA Bulletin 134:1549-1570.

Rodríguez-Méndez L, Cuevas J, Esteban JJ, Tubía JM, Sergeev S, Larionov A (2014) Age of the magmatism related to the inverted Stephanian–Permian basin of the Sallent area (Pyrenees). Geol Soc, London, Spec Publ 394:101-111.

Roger F, Respaut JP, Brunal M, Matte P, Paquette JL (2004) Première datation U–Pb des orthogneiss oeillés de la zone axiale de la Montagne noire (Sud du Massif central) : nouveaux témoins du magmatisme ordovicien dans la chaîne Varisque. CR Geosci 336:19-28.

Roger F, Teyssier C, Respaut JP et al (2015) Timing of formation and exhumation of the Montagne Noire double dome, French Massif Central. Tectonophysics 640-641:53-69.

Roger F, Teyssier C, Whitney DL, Respaut JP, Paquette JL, Rey PF (2020) Age of metamorphism and deformation in the Montagne Noire dome (French Massif Central): Tapping into the memory of fine-grained gneisses using monazite U-Th-Pb geochronology. Tectonophysics 776. doi.org/10.1016/j.tecto.2019.228316

Román-Berdiel T, Casas AM, Oliva-Urcia B, Pueyo EL, Liesa C, Soto R (2006) The Variscan Millares granite (central Pyrenees): Pluton emplacement in a T fracture of a dextral shear zone. Geodin Acta 19: 197–211.

Schnapperelle S, Mezger JE, Stipp M, Hofmann M, Gärtner A, Linnemann U (2020) Polyphase magmatic pulses along the Northern Gondwana margin: U-Pb zircon geochronology from gneiss domes of the Pyrenees. Gondwana Res 81:291-311.

Schulmann K, Lexa O, Stipska P et al. (2008) Vertical extrusion and horizontal channel flow of orogenic lower crust: key exhumation mechanisms in large hot orogens? J Metamorph Geol 26:273–297.

Schulmann K, Catalán JRM, Lardeaux JM, Janousek V, Oggiano G (2014) The Variscan orogeny: extent, timescale and the formation of the European crust. Geol. Soc. Lond. Spec. Publ. 405: 1–6.

Siron G, Goncalves P, Marquer D, Pierre T, Paquette JL, Vanardois J (2020) Contribution of magmatism, partial melting buffering and localized crustal thinning on the late-Variscan thermal structure of the Agly massif (French Pyrenees). J Metamorph Geol 38: 799-829

Steiger RH, Jäger E (1977) Subcommission on geochronology: convention on the use of decay constants in geo- and cosmochronology. Earth Planet Sci Lett 36:359–362

Stephan T, Kroner UWE, Romer RL (2019) The pre-orogenic detrital zircon record of the Peri-Gondwanan crust. Geol Mag 156-281-307.

Teipel U, Eichhorn R, Loth G, Rohrmüller J, Höll R, Kennedy A (2004) U-Pb SHRIMP and Nd isotopic data from the western Bohemian Massif (Bayerischer Wald, Germany): implications for upper Vendian and lower Ordovician magmatism. Int J Earth Sci 93:782-801.

Tournaire Guille B, Olivier P, Paquette JL, Bosse V, Guillaume D (2019) Evolution of the middle crust of the Pyrenees during the Paleozoic: new data on the plutonic rocks from the North Pyrenean Agly Massif. Int J Earth Sci 108:245-265.

Townsend KJ, Miller CF, D'Andrea JL, Ayers JC, Harrison TM, Coath CD (2000). Low temperature replacement of monazite in the Ireteba granite, southern Nevada: geochronological implications. Chem Geol 172:95-112

Trap P, Roger F, Cenki-Tok B, Paquette JL (2017) Timing and duration of partial melting and magmatism in the Variscan Montagne Noire gneiss dome (French Massif Central). Int J Earth Sci 106:453–476.

Vacherat A, Mouthereau F, Pik R et al (2017) Rift-to-collision sediment routing in the Pyrenees: A synthesis from sedimentological, geochronological and kinematic constraints. Earth Sci Rev 172:43-72.

van Achterbergh E, Ryan CG, Jackson SE, Griffin WL (2001) Data reduction software for LA-ICP-MS. In: Sylvester P (ed) Laser ablation-ICPMS in the earth science. Mineralogical Association of Canada. Vol. 29, 239-243.

Van Lichtervelde M, Grand'Homme A, de Saint-Blanquat M, Olivier P, Gerdes A, Paquette JL, Melgarejo JC, Druguet E, Alfonso, P. (2017). U-Pb geochronology on zircon and columbite-group minerals of the Cap de Creus pegmatites, NE Spain. Mineral petrol 111:1-21.

Vanardois J, Trap P, Goncalves P et al (2020) Kinematics, deformation partitioning and late Variscan magmatism in the Agly massif, Eastern Pyrenees, France. Bull Soc Geol Fr 191. doi.org/10.1051/bsgf/2020009

Vanderhaeghe O, Laurent O, Gardien, V et al (2020) Flow of partially molten crust controlling construction, growth and collapse of the Variscan orogenic belt: the geologic record of the French Massif Central. Bull Soc Géol Fr 191, doi.org/10.1051/bsgf/2020013.

Vielzeuf D (1984) Relations de phases dans le faciès granulite et implications géodynamiques. L'exemple des granulites des Pyrénées. State thesis, Clermont-Ferrand (France): Univ. Blaise Pascal.

Vielzeuf D, Paquette JL, Clemens JD, Stevens G, Gannoun A, Suchorski K, Saúl A (2021) Age, duration and mineral markers of magma interactions in the deep crust: an example from the Pyrenees. Contrib Mineral Petrol. doi.org/10.1007/s00410-021-01789-2

Von Raumer JF, Stampfli GM, Arenas R, Martínez SS (2015) Ediacaran to Cambrian oceanic rocks of the Gondwana margin and their tectonic interpretation. Int J Earth Sci 104:1107–1121.

Whitney DL, Teyssier C, Rey P, Buck WR (2013) Continental and oceanic core complexes. GSA Bulletin 125:273-298.

Whitney DL, Roger F, Teyssier C, Rey PF, Respaut JP. 2015. Syncollapse eclogite metamorphism and exhumation of deep crust in a migmatite dome: The P–T–t record of the youngest Variscan eclogite (Montagne Noire, French Massif Central). Earth Planet Sci Lett 430: 224–234

Whitney DL, Hamelin C, Teyssier C, Raia NH, Korchinski MS, Seaton NC, von der Handt A, Roger F, Rey, PF. 2020. Deep crustal source of gneiss dome revealed by eclogite in migmatite (Montagne Noire, French Massif Central). J Metamorph Geol 38:297-327.

## Figures captions:

**Fig. 1 a** Paleogeographic reconstruction of the Variscan Belt during Late Carboniferous modified from Cochelin et al. (2021). **b** Simplified cross-section from the southern edge of the French Central Massif showing the lateral flow of the partially molten crust, modified from Vanderhaeghe et al. (2020). FCM: French Central Massif; MN: Montagne Noire; NPF: North Pyrenean Fault; NPZ: North Pyrenean Zone; PAZ: Pyrenean Axial Zone.

**Fig. 2** Geological map of the Agly massif with localisation of the dated samples.

**Fig. 3 a** Structural map and **b** cross-sections of the Agly massif modified from Vanardois et al. (2020). Dated samples are located on the map and cross-sections.

**Fig. 4** Structural evidence of D1, D2 and D3 planar fabrics in the Agly massif. S1 foliations affected by F2 folds **a** in the migmatitic basement and **b** in the schists. **c** and **d** C-S structures showing top-to-the-north kinematics in high-D2 strain domains from the migmatitic basement. S2 foliations affected by F3 folds with S3 vertical axial planes **e** in gneiss and **f** in anatectic micaschists.

**Fig. 5 a** Monazite U-Th-Pb concordia diagram and **b** zircon U-Pb Tera Wasserburg diagram obtained by LA-ICPMS on the Vivier leucogranite (Ag57). Error ellipses and uncertainties in ages are ± 2σ.

Dotted ellipses are not taken into account for the age calculation. $MSWD_{(C+E)}$: Mean Square of Weighted Deviates for Concordance and Equivalence.

**Fig. 6** Locations and morphologies in BSE images of monazite from the Dam migmatitic paragneiss (Ag3B). **a** Thin section of the dam migmatitic paragneiss (Ag3B) with the three textural domains where monazite grains are located: **b** in the matrix, **c** and **d** within the garnet, **e** and **f** in the deformed zone. Red circles indicate laser spot analyses with a diameter of 12 µm and red numbers correspond to single-analysis concordia age obtained on the different monazite analysed (in white the grain numbers). The data reported in Table S3.

**Fig. 7** Monazite U-Th-Pb concordia diagrams of the Dam migmatitic paragneiss Ag3B. Monazite grains within **a** the matrix, **b** the garnet, **c** the deformed zone and **d** all data. Error ellipses and uncertainties on ages are ± 2σ. Dotted ellipses are not taken into account only for the age calculation.

**Fig. 8** Field relations of the Brosse Ravine pegmatites (Ag03 and Ag38). **a** Cross-section passing by the boundary of the infra- and suprastructure marked by the Caladroy Shear Zone (CSZ), location on Fig. 2 and 3A. **b** Cross-section of the Brosse Ravine. Outcrop photographs of the Brosse ravine pegmatites: **c** Ag03 cross-cutting S2 foliations and bearing a xenolith of micaschist and **d** Ag38 with L2 stretching lineation marked by tourmalines (RHR orientation).

**Fig. 9** Monazite U-Th-Pb concordia diagrams (**a** and **c**) and zircon Tera Wasserburg diagrams (**b** and **d**) of the Brosse ravine pegmatites Ag03 and Ag38. Error ellipses and uncertainties in ages are ± 2σ. In the **a**, **c** and **d** diagrams, the dotted ellipses are taken into account for the concordia age calculation while in diagram **b** these are the white ellipses.

**Fig. 10** Zircon U-Pb Tera Wasserburg diagram obtained by LA-ICPMS on the Planèzes pegmatite (Ag47). Error ellipses and uncertainties in ages are ± 2σ. Dotted ellipses are not taken into account for the age calculation.

**Fig. 11** Microphotographs and field relations from samples within the D3 corridor and from the two Tournefort dykes. **a** Foliations map of the Tournefort area modified from Vanardois et al. (2020). S4 is a local planar fabric induced by the emplacement of the Saint-Arnac pluton. **b** Outcrop photograph from the Tournefort pegmatite (Ag08) and its relation with de Proto-S3 magmatic foliation of the Tournefort diorite. **c** Leucogranite dyke (Ag06) thin section showing no marked deformation. *Kfs*: K-feldspar – *Qtz*: quartz – *Grt*: garnet – *Bt*: biotite – *Ms*: muscovite – *Pl*: plagioclase – *Myr*: myrmekite – *Sill*: sillimanite.

**Fig. 12** Monazite U-Th-Pb concordia diagrams (**a** and **c**) and zircon Tera Wasserburg diagrams (**b** and **d**) of the Tournefort pegmatite (Ag08) and of the Tournefort leucogranite (Ag06). Error ellipses and uncertainties on ages are $\pm 2\sigma$. Dotted ellipses are not taken into account only for the age calculation. In **a** and **c**, Mn 13 and Mn10 are not plotted because they are outside the ranges, respectively.

**Fig. 13 a** Monazite U-Th-Pb concordia diagram and **b** zircon U-Pb Tera Wasserburg a diagram obtained by LA-ICPMS on the Vivier orthogneiss (Ag48). Error ellipses and uncertainties in ages are $\pm 2\sigma$. White ellipses are discordant data and are not taken into account in the histogram diagram and for the age calculation, while dotted ellipses are not taken into account only when calculating the concordia age.

**Fig. 14 a** Ag51 Latour-de-France Leucogranite thin section presenting myrmekites, plastic quartz deformation and recrystallization. **b** Monazite U-Th-Pb concordia diagram and **c** zircon Tera Wasserburg diagram of the Latour-de-France leucogranite (Ag51). Error ellipses and uncertainties on ages are $\pm 2\sigma$. Dotted ellipses are not taken into account only for the age calculation.

**Fig. 15** Compilation of ages from the Agly massif constraining deformations and/or metamorphism and tectonic evolution. References: (1) Tournaire Guille et al. 2019; (2) Olivier et al. 2004; (3) Postaire 1982; (4) Respaut and Lancelot 1983; (5) Siron et al. 2020; (6) Olivier et al. 2008; (7) This study. Geochronological data from Odlum and Stockli (2019) were not processed to decipher Variscan tectonics and are not included in this compilation. *Basic Ansi. charno. facies:* Basic Ansignan charnockite facies – *Leuco. Ansi. charno. facies:* Leucocrate Ansignan charnockite facies.

**Fig. 16** Tectonic model showing the strain partitioning between D2 extensive structures and D3 dextral wrenching between 325 and 300 Ma. **a** Beginning of D2 deformation in suprasolidus conditions associated to horizontal flow of the lower crust around 325 Ma forming a S2 foliation transposing former S1 foliation. **b** Beginning of the strain partitioning between the extensive S2 and C2 structures and the early proto-D3 dextral wrenching draining the Tournefort diorite. **c** Ongoing melt draining in the D3 dextral wrenching forms the Saint-Arnac granite, inducing local strain interference preserving proto-S3 foliations in the Tournefort area and localizing late-D2 at its edges. In **b** and **c**, the Tournefort diorite and Saint-Arnac granite are duplicated to illustrate 3D geometry.

**Fig. 17** Tectonic evolution of the southern edge of the Variscan orogenic plateau. **a** A lateral gravity-driven flow of the molten infrastructure (in orange) below the suprastructure (in blue) took place from the French Central Massif (FCM) to the Pyrenees between ca. 325 and 310 Ma. **b** Around 308 Ma, the pervasive transcurrent deformation in the PAZ and MN reoriented the flow of the infrastructure, while in low-transcurrent domains, i.e. NPZ and FCM, the gravity driven flow continued. **c** At ca. 300 Ma, most of the anatectic melts of the infrastructure crystallized and the flow of the infrastructure stopped. The transcurrent setting was active until ca. 290 Ma with numerous dextral shear zones in the PAZ and MN, and local ones in the NPZ and FCM. See text for details.

**Table 1:** Summary of geographic location, rock types, and U-Th-Pb geochronological results for samples analysed in this study. (Zr): zircon age; (Mn): monazite age; T.S.: monazite age obtained on thin section.

## Supplementary material

**Table S1:** Operating conditions and instrument settings for LA-ICPMS U-Th-Pb analyses.

**Table S2:** Analytical results of LA-ICPMS U-Th-Pb dating on monazite. Mn: monazite; R: rim; C: centre. Errors quoted in absolute values. Textural position of monazite analyzed in situ (T.S., thin section) from sample Ag3B. in Bt: included in biotite; in Sill.: included in sillimanite; in matrix: included in the quartzo-feldspathic matrix.

**Table S3:** Analytical results of LA-ICPMS U-Pb dating on zircon. Zr: zircon; R: rim; C: centre.

**Fig. S1**: Monazite morphologies in BSE images. Red circles indicate laser spot locations and $^{208}Pb/^{232}Th$ age without error associated.

**Fig. S2**: Zircon morphologies in CL images for Ag57, Ag48, Ag47, Ag51, Ag38 and Ag03, and in BSE images for Ag06 and Ag08. Red circles indicate laser spot locations and age without errors associated.

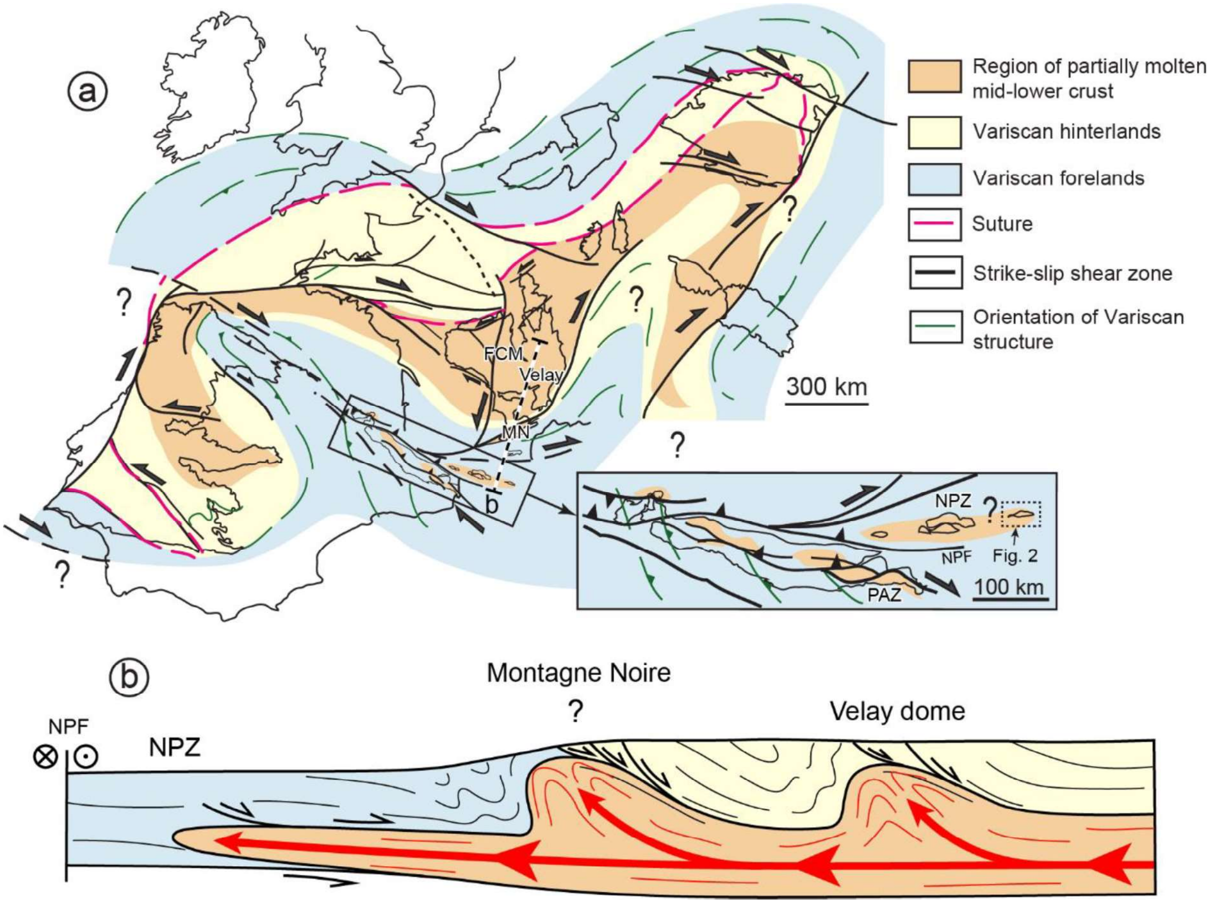


Fig. 1

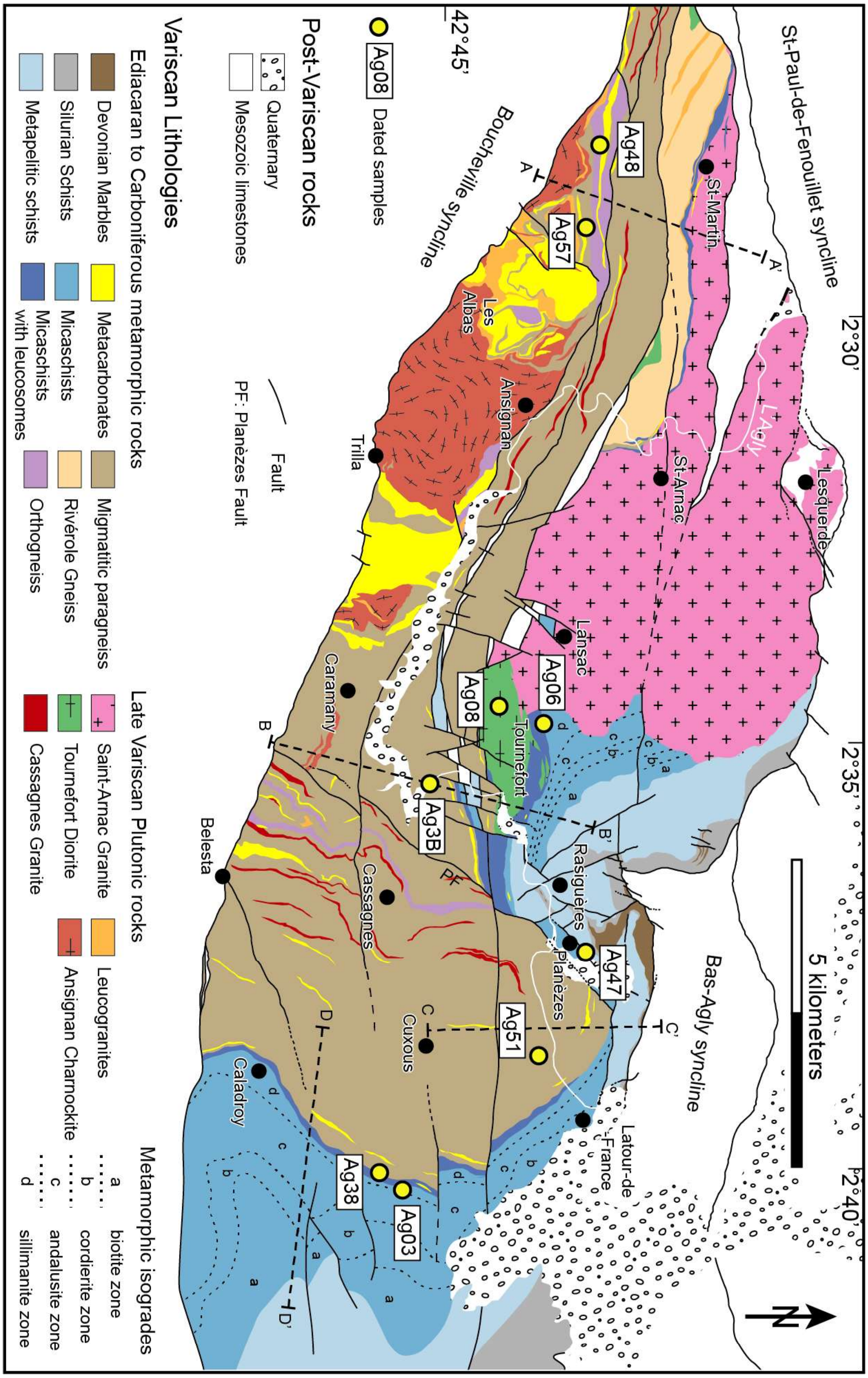

St-Paul-de-Fenouillet syncline
Bas-Agly syncline
Boucheville syncline
5 kilometers
2°30'
2°35'
2°40'
42°45'
N
St-Martin
St-Arnac
Lesquerde
L'Agly
Ansignan
Les Albas
Trilla
Lansac
Tournefort
Caramany
Rasiguères
Planèzes
Cassagnes
Belesta
Cuxous
Latour-de-France
Caladroy
PF
A
A'
B
B'
C
C'
D
D'
Ag48
Ag57
Ag06
Ag08
Ag3B
Ag47
Ag51
Ag38
Ag03
Ag08 Dated samples
Post-Variscan rocks
Quaternary
Mesozoic limestones
Fault
PF: Planèzes Fault
Variscan Lithologies
Ediacaran to Carboniferous metamorphic rocks
Devonian Marbles
Silurian Schists
Metapelitic schists
Metacarbonates
Micaschists
Micaschists with leucosomes
Migmatitic paragneiss
Rivérole Gneiss
Orthogneiss
Late Variscan Plutonic rocks
Saint-Arnac Granite
Tournefort Diorite
Cassagnes Granite
Leucogranites
Ansignan Charnockite
Metamorphic isogrades
a biotite zone
b cordierite zone
c andalusite zone
d sillimanite zone


Fig. 2

1152

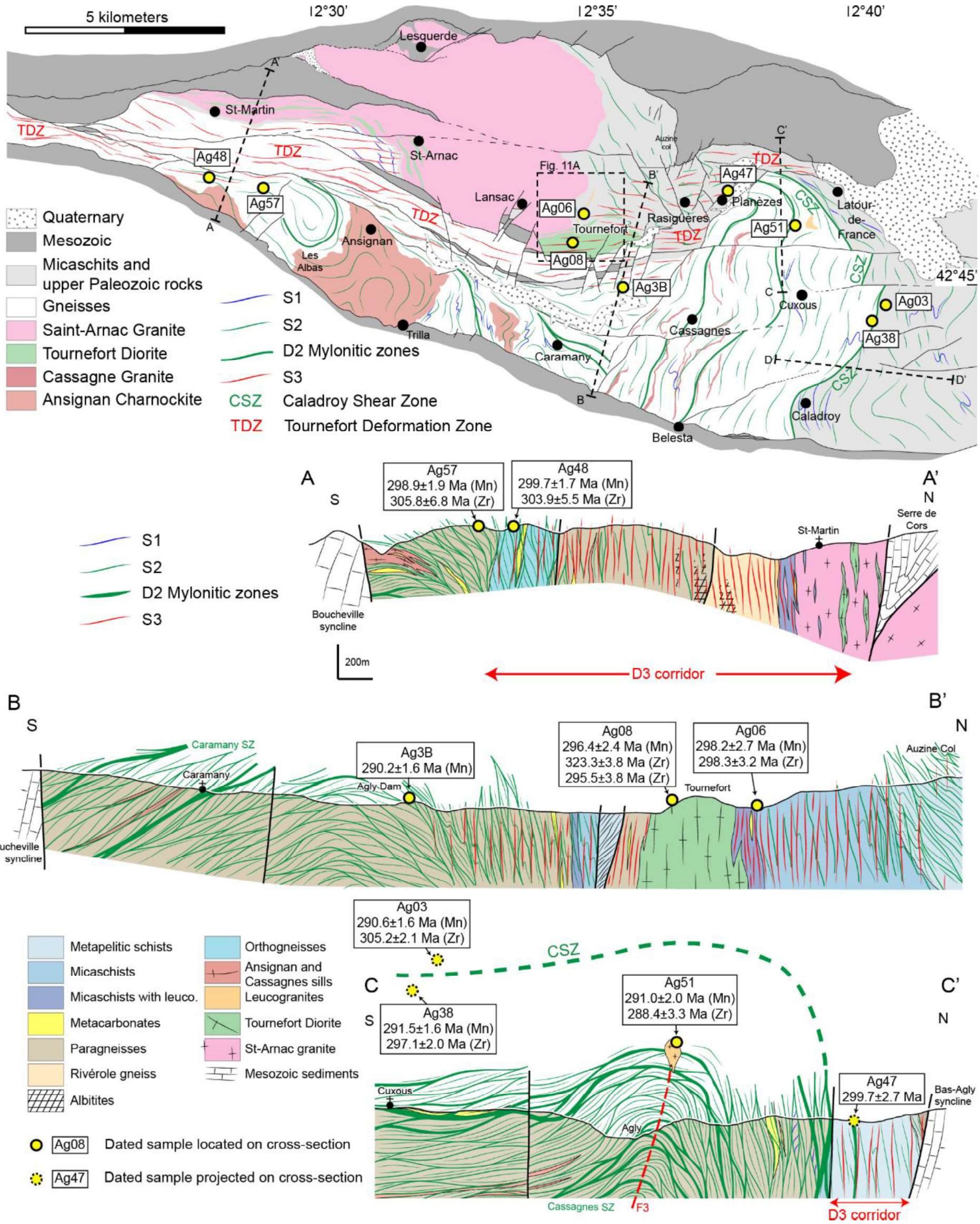


1153 Fig. 3

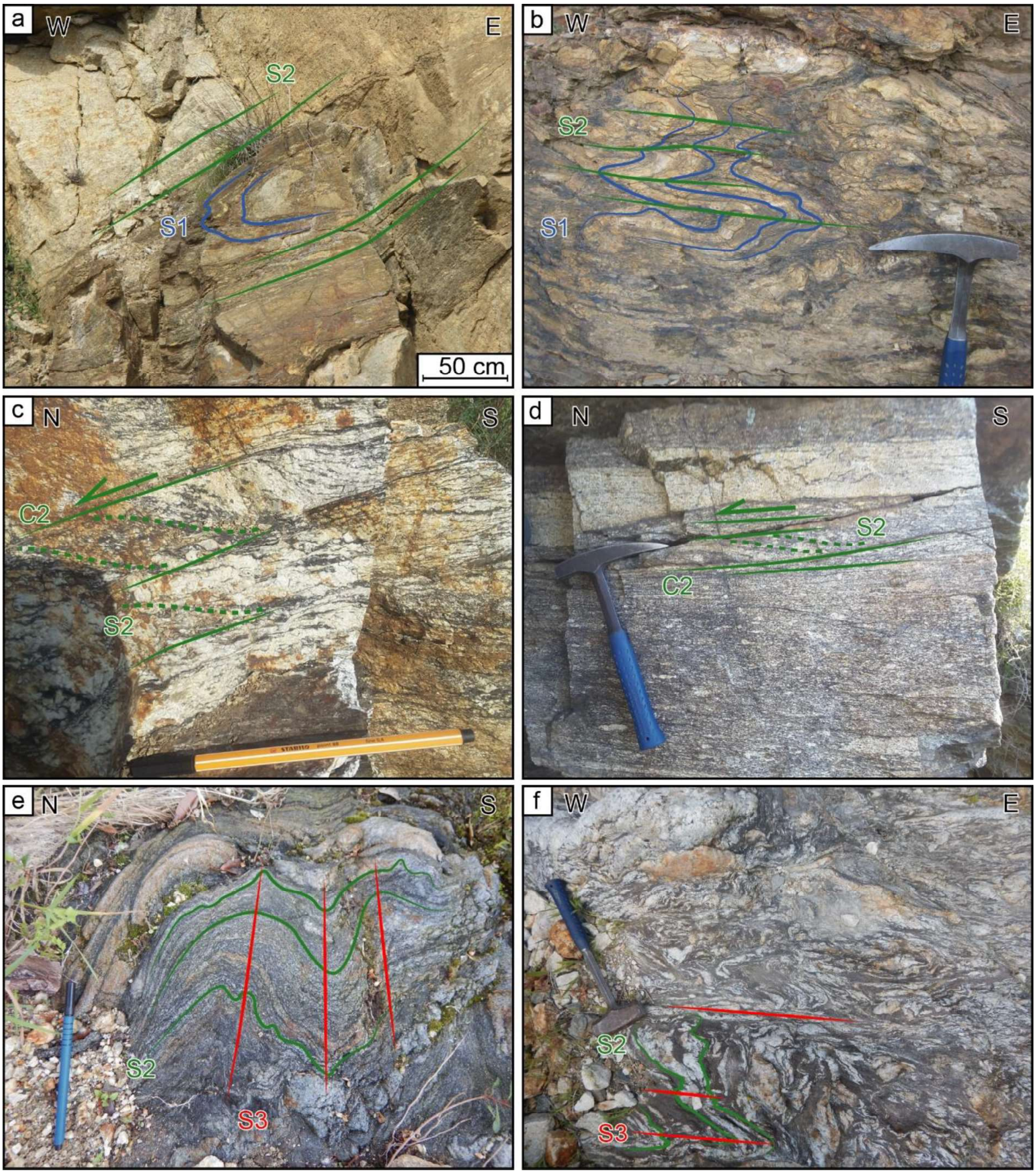

1154

1155 Fig. 4

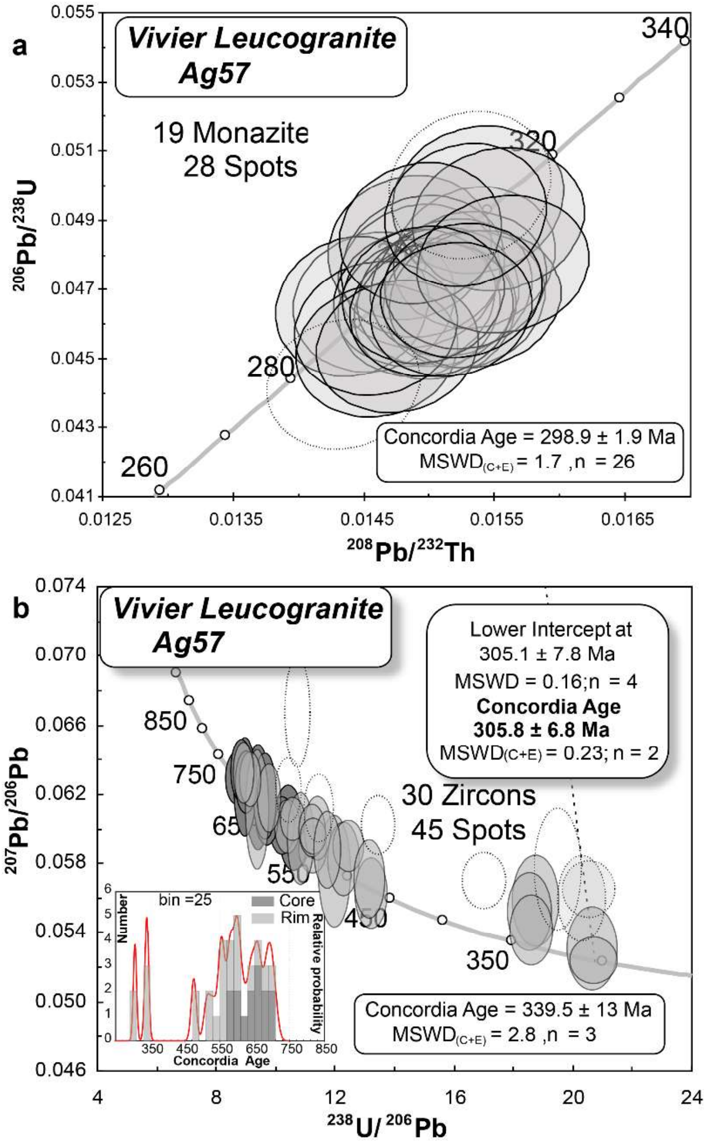


1156

1157 Fig. 5

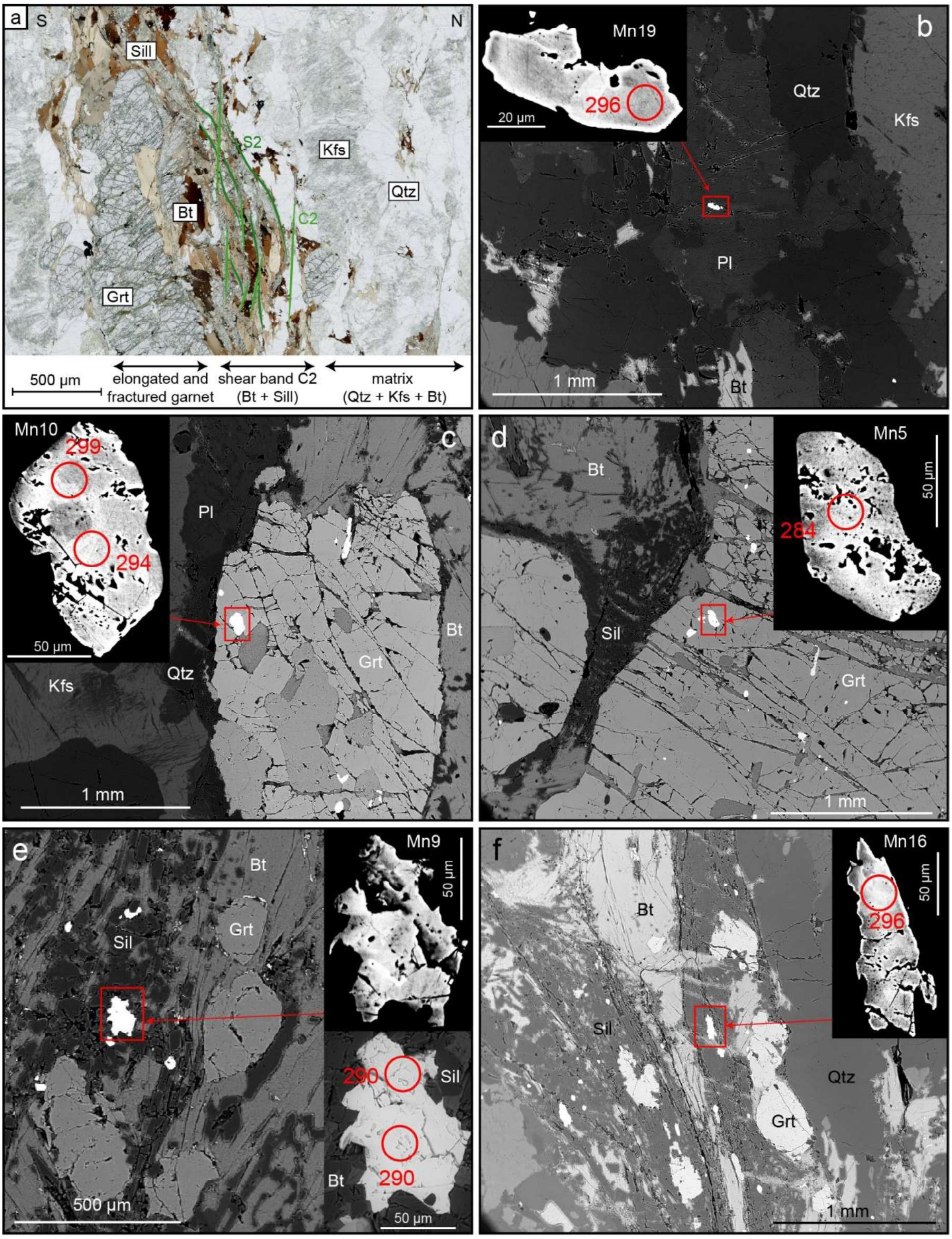


1158

1159 Fig. 6

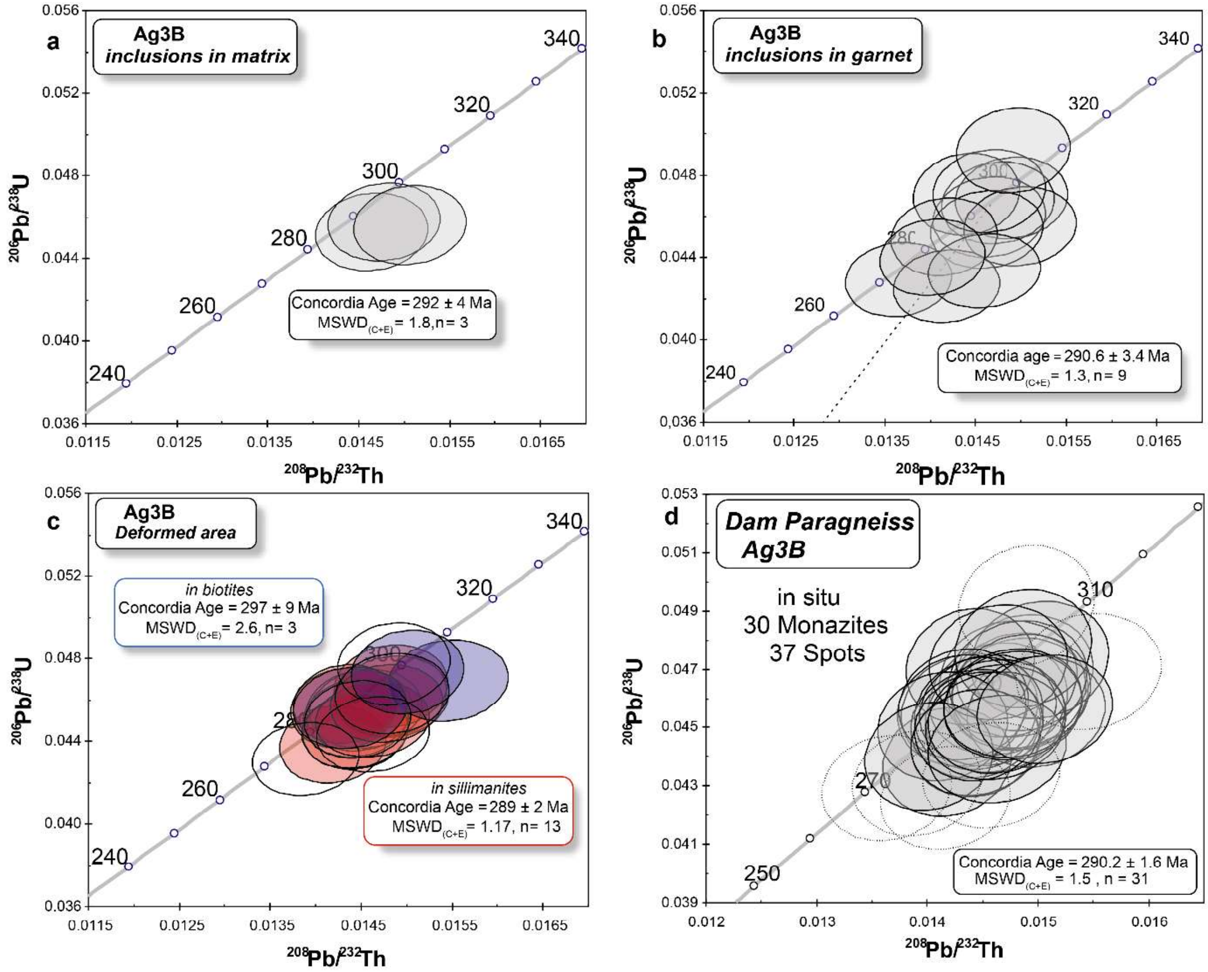


1160

1161 Fig. 7

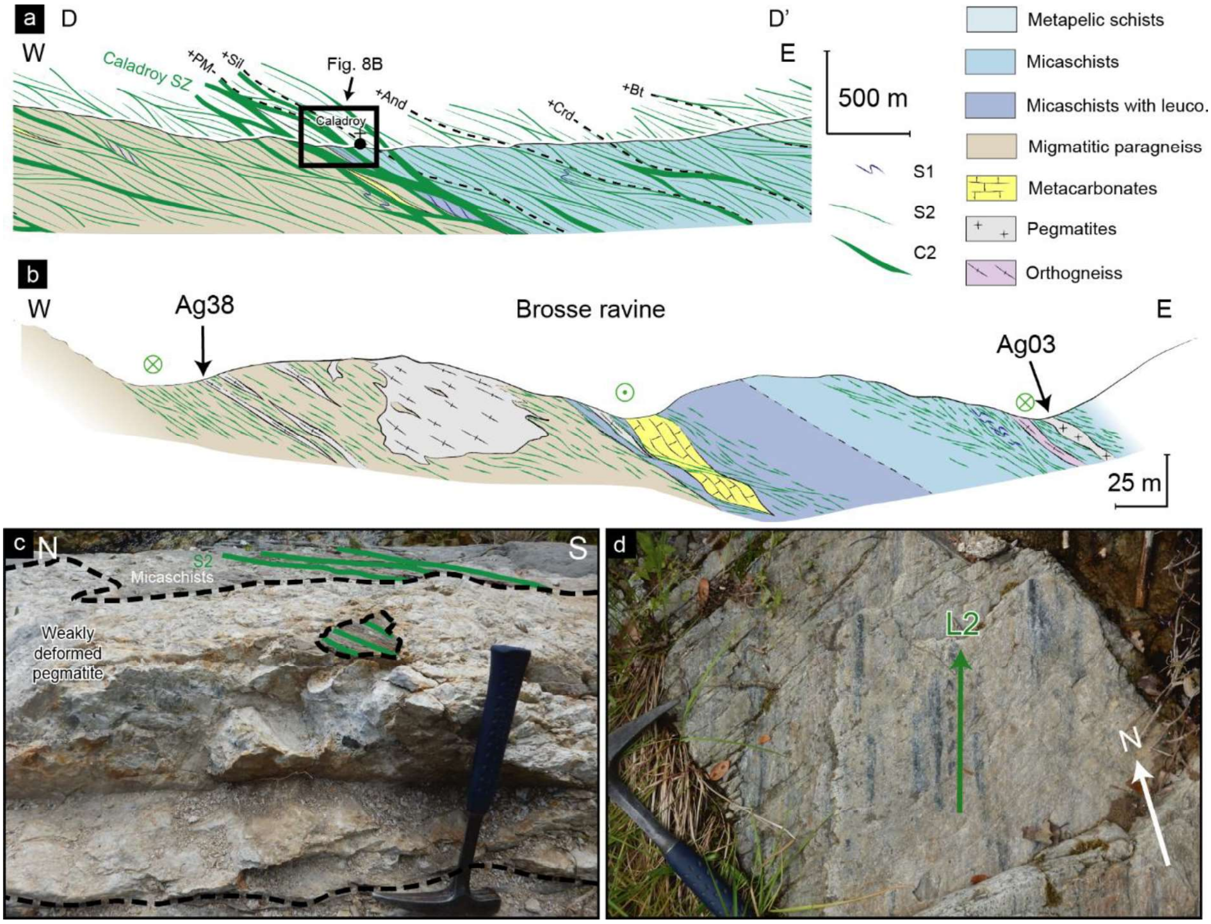


1162

1163 Fig. 8

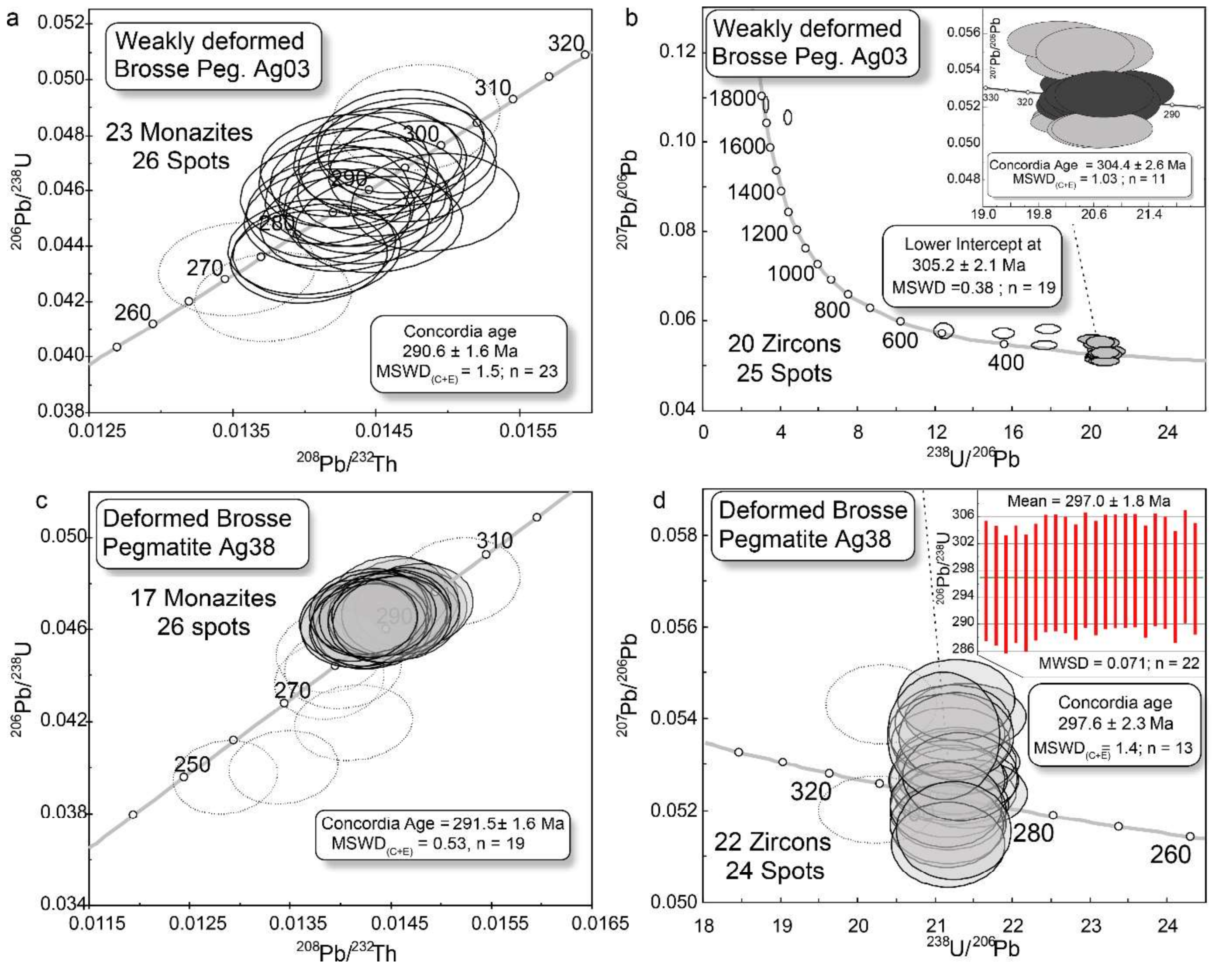
a
Weakly deformed
Brosse Peg. Ag03
23 Monazites
26 Spots
Concordia age
290.6 ± 1.6 Ma
MSWD(C+E) = 1.5; n = 23
206Pb/238U
208Pb/232Th
b
Weakly deformed
Brosse Peg. Ag03
Concordia Age = 304.4 ± 2.6 Ma
MSWD(C+E) = 1.03 ; n = 11
Lower Intercept at
305.2 ± 2.1 Ma
MSWD =0.38 ; n = 19
20 Zircons
25 Spots
207Pb/206Pb
238U/206Pb
c
Deformed Brosse
Pegmatite Ag38
17 Monazites
26 spots
Concordia Age = 291.5± 1.6 Ma
MSWD(C+E) = 0.53, n = 19
206Pb/238U
208Pb/232Th
d
Deformed Brosse
Pegmatite Ag38
Mean = 297.0 ± 1.8 Ma
MWSD = 0.071; n = 22
Concordia age
297.6 ± 2.3 Ma
MSWD(C+E) = 1.4; n = 13
22 Zircons
24 Spots
207Pb/206Pb
238U/206Pb

Fig. 9

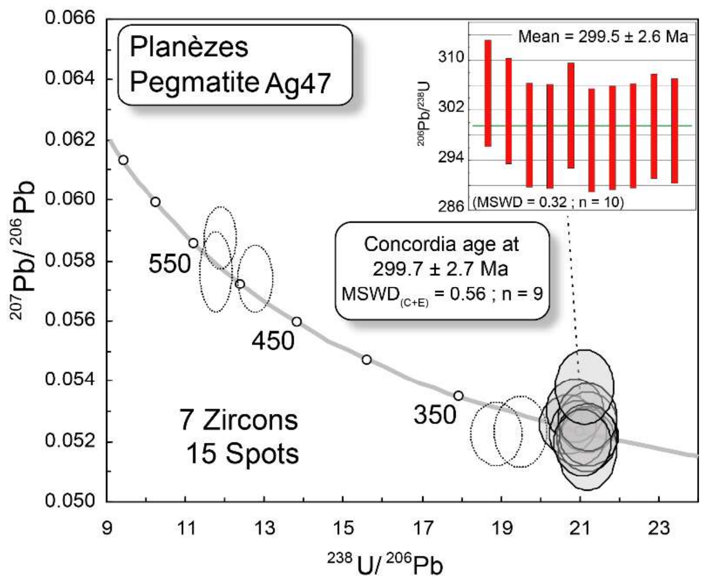
Planèzes
Pegmatite Ag47
Mean = 299.5 ± 2.6 Ma
(MSWD = 0.32 ; n = 10)
Concordia age at
299.7 ± 2.7 Ma
MSWD(C+E) = 0.56 ; n = 9
7 Zircons
15 Spots
207Pb/206Pb
238U/206Pb

Fig. 10

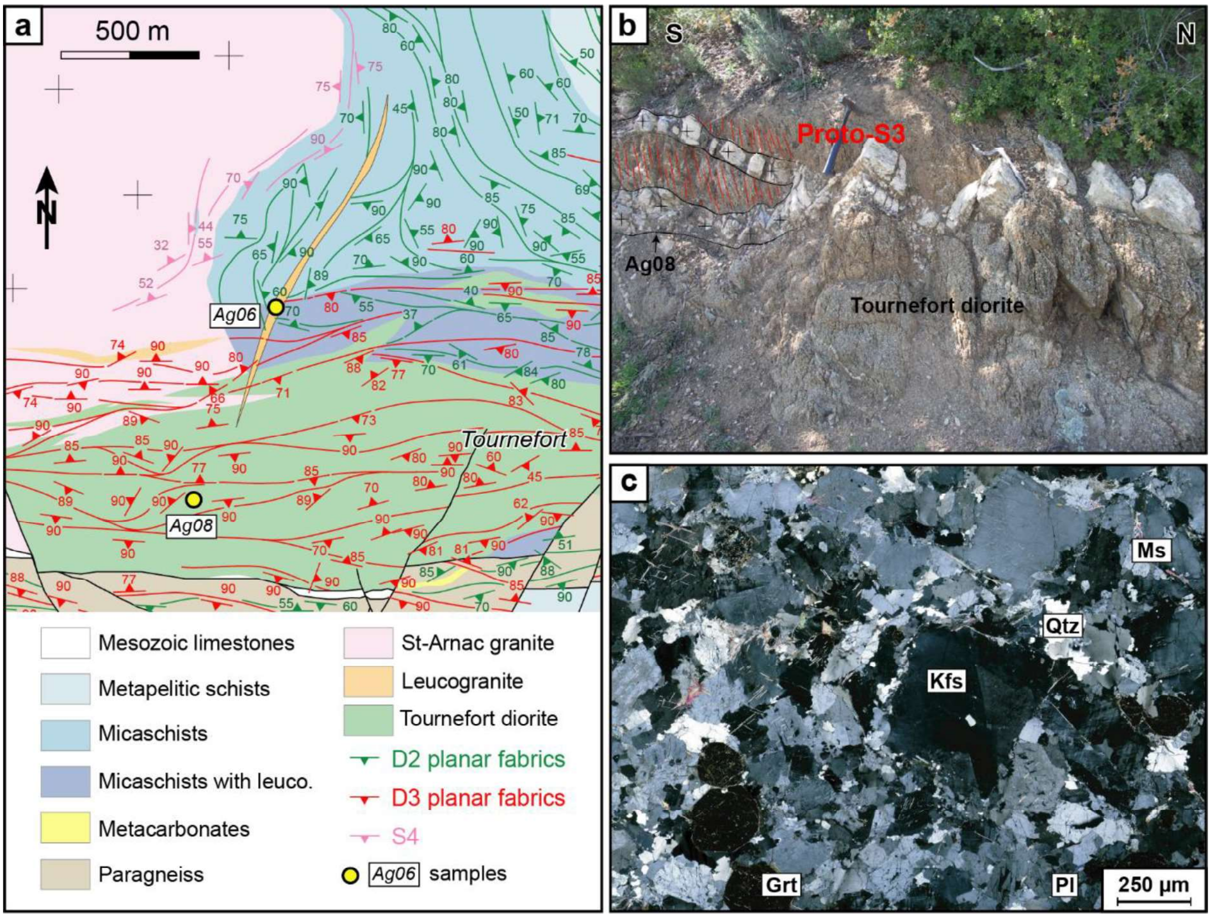
a
500 m
N
Ag06
Ag08
Tournefort
Mesozoic limestones
Metapelitic schists
Micaschists
Micaschists with leuco.
Metacarbonates
Paragneiss
St-Arnac granite
Leucogranite
Tournefort diorite
D2 planar fabrics
D3 planar fabrics
S4
Ag06 samples
b
S
N
Proto-S3
Ag08
Tournefort diorite
c
Ms
Qtz
Kfs
Grt
Pl
250 µm

Fig. 11

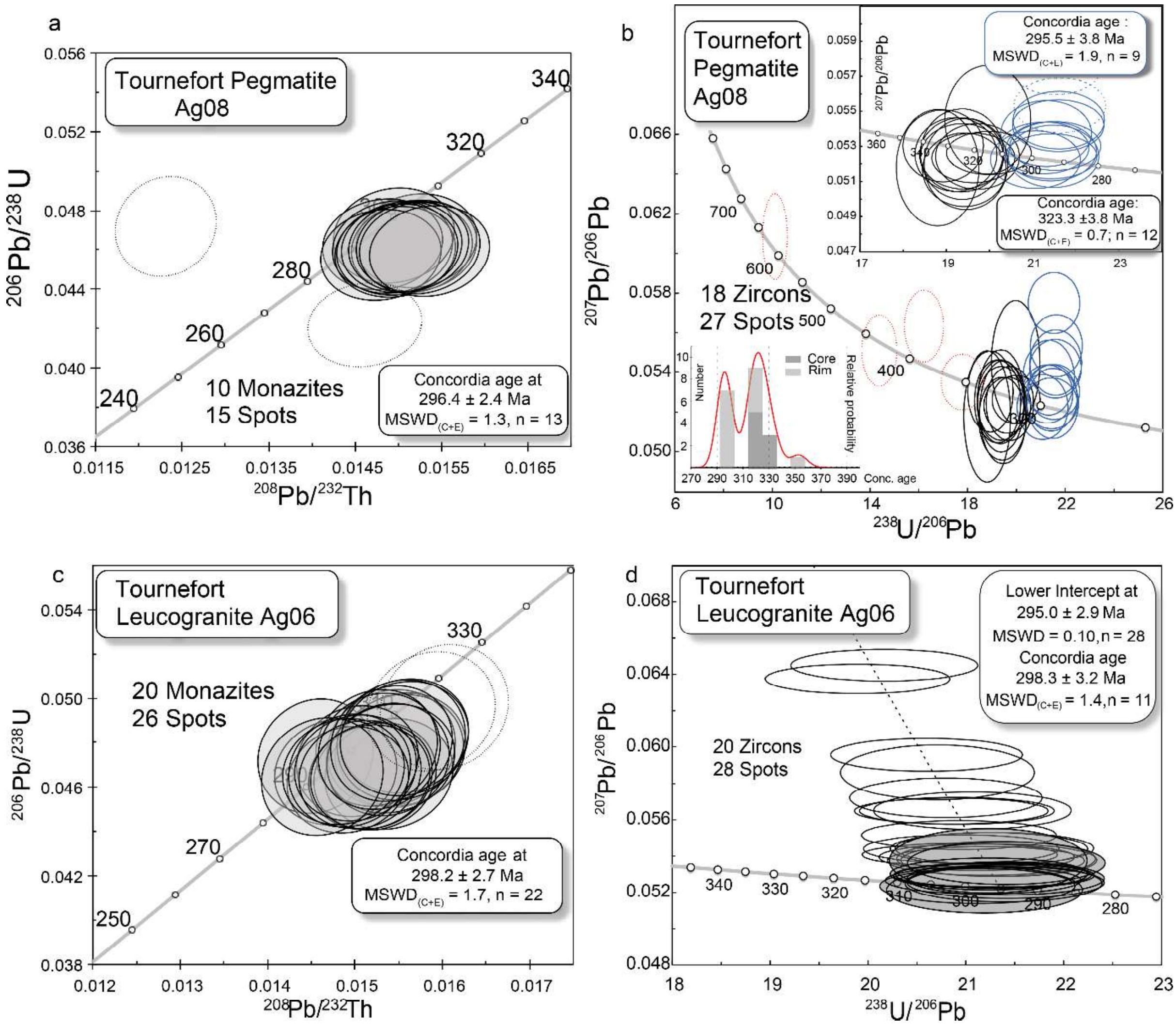
a
Tournefort Pegmatite
Ag08
10 Monazites
15 Spots
Concordia age at
296.4 ± 2.4 Ma
MSWD(C+E) = 1.3, n = 13
206Pb/238U
208Pb/232Th
b
Tournefort
Pegmatite
Ag08
18 Zircons
27 Spots
Concordia age :
295.5 ± 3.8 Ma
MSWD(C+L) = 1.9, n = 9
Concordia age:
323.3 ±3.8 Ma
MSWD(C+F) = 0.7; n = 12
Core
Rim
Number
Relative probability
Conc. age
207Pb/206Pb
238U/206Pb
c
Tournefort
Leucogranite Ag06
20 Monazites
26 Spots
Concordia age at
298.2 ± 2.7 Ma
MSWD(C+E) = 1.7, n = 22
206Pb/238U
208Pb/232Th
d
Tournefort
Leucogranite Ag06
Lower Intercept at
295.0 ± 2.9 Ma
MSWD = 0.10, n = 28
Concordia age
298.3 ± 3.2 Ma
MSWD(C+E) = 1.4, n = 11
20 Zircons
28 Spots
207Pb/206Pb
238U/206Pb

Fig. 12

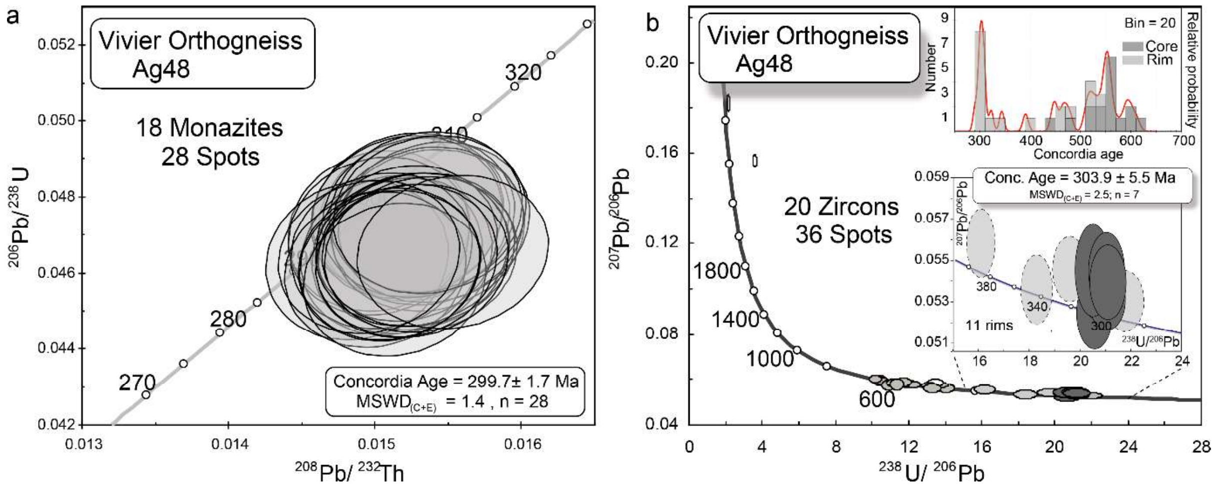
a
Vivier Orthogneiss
Ag48
18 Monazites
28 Spots
Concordia Age = 299.7± 1.7 Ma
MSWD(C+E) = 1.4 , n = 28
206Pb/238U
208Pb/ 232Th
b
Vivier Orthogneiss
Ag48
20 Zircons
36 Spots
Bin = 20
Core
Rim
Number
Relative probability
Concordia age
Conc. Age = 303.9 ± 5.5 Ma
MSWD(C+E) = 2.5; n = 7
11 rims
207Pb/206Pb
238U/ 206Pb

Fig. 13

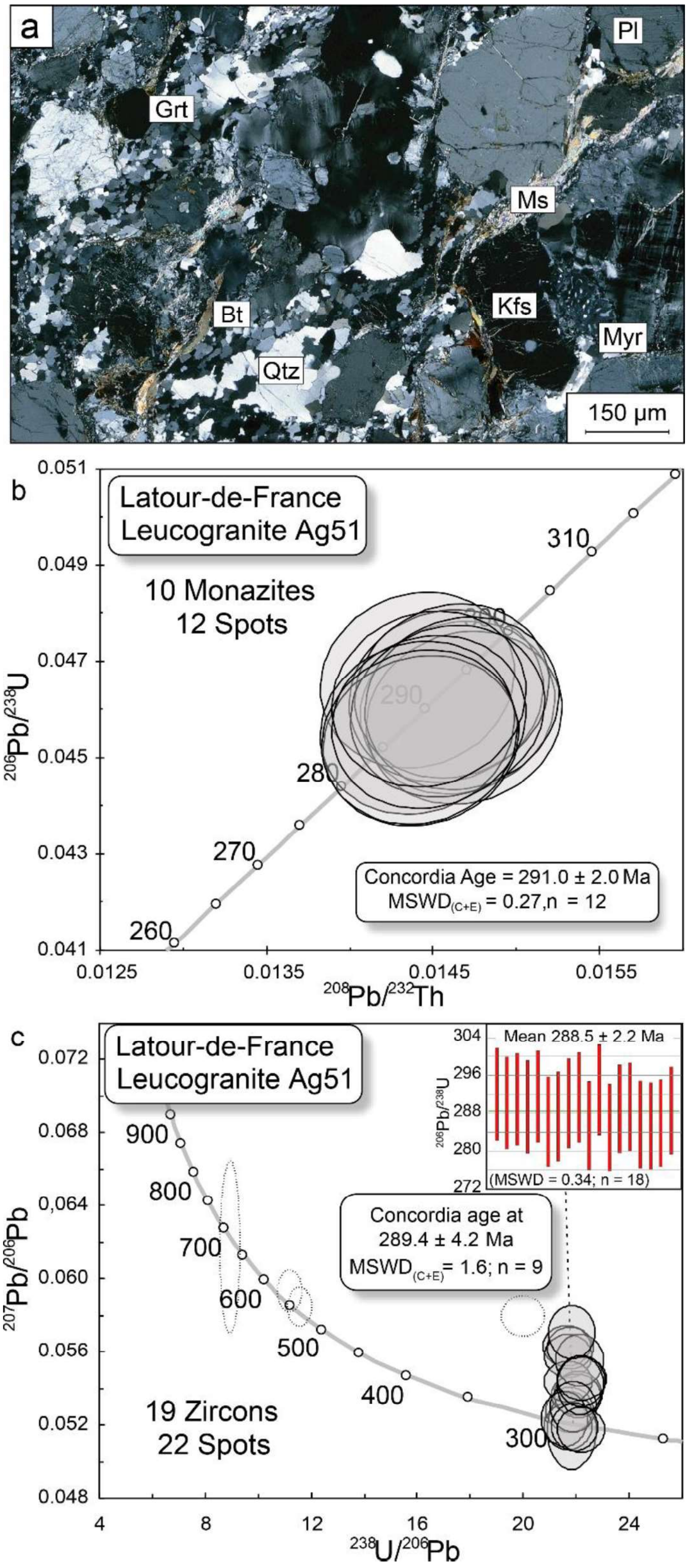
a
Pl
Grt
Ms
Kfs
Bt
Myr
Qtz
150 µm
b
Latour-de-France
Leucogranite Ag51
10 Monazites
12 Spots
310
290
280
270
260
Concordia Age = 291.0 ± 2.0 Ma
MSWD(C+E) = 0.27,n = 12
206Pb/238U
208Pb/232Th
0.051
0.049
0.047
0.045
0.043
0.041
0.0125
0.0135
0.0145
0.0155
c
Latour-de-France
Leucogranite Ag51
Mean 288.5 ± 2.2 Ma
(MSWD = 0.34; n = 18)
304
296
288
280
272
Concordia age at
289.4 ± 4.2 Ma
MSWD(C+E)= 1.6; n = 9
900
800
700
600
500
400
300
19 Zircons
22 Spots
207Pb/206Pb
238U/206Pb
0.072
0.068
0,064
0.060
0.056
0.052
0.048
4
8
12
16
20
24

Fig. 14

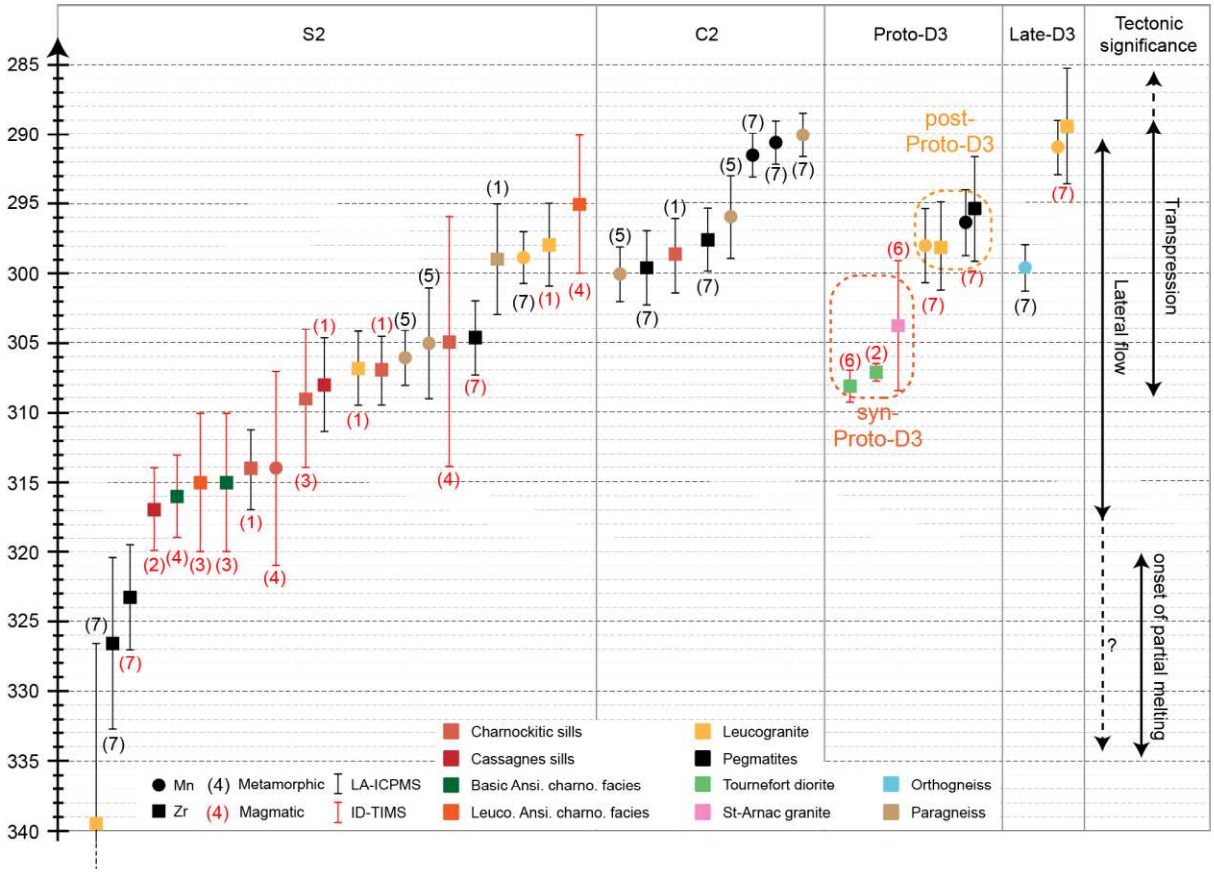
S2
C2
Proto-D3
Late-D3
Tectonic significance
post-Proto-D3
syn-Proto-D3
Transpression
Lateral flow
onset of partial melting
Mn
Zr
(4) Metamorphic
(4) Magmatic
LA-ICPMS
ID-TIMS
Charnockitic sills
Cassagnes sills
Basic Ansi. charno. facies
Leuco. Ansi. charno. facies
Leucogranite
Pegmatites
Tournefort diorite
St-Arnac granite
Orthogneiss
Paragneiss

Fig. 15

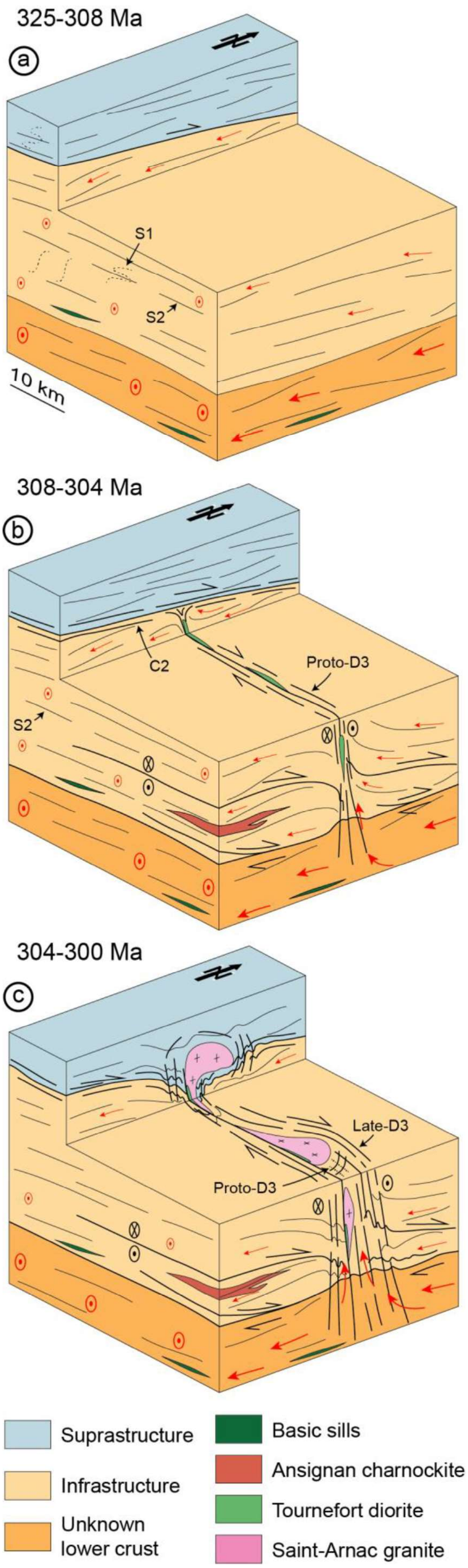
325-308 Ma
a
S1
S2
10 km
308-304 Ma
b
C2
Proto-D3
S2
304-300 Ma
c
Late-D3
Proto-D3
Suprastructure
Infrastructure
Unknown
lower crust
Basic sills
Ansignan charnockite
Tournefort diorite
Saint-Arnac granite

1179

Fig. 16

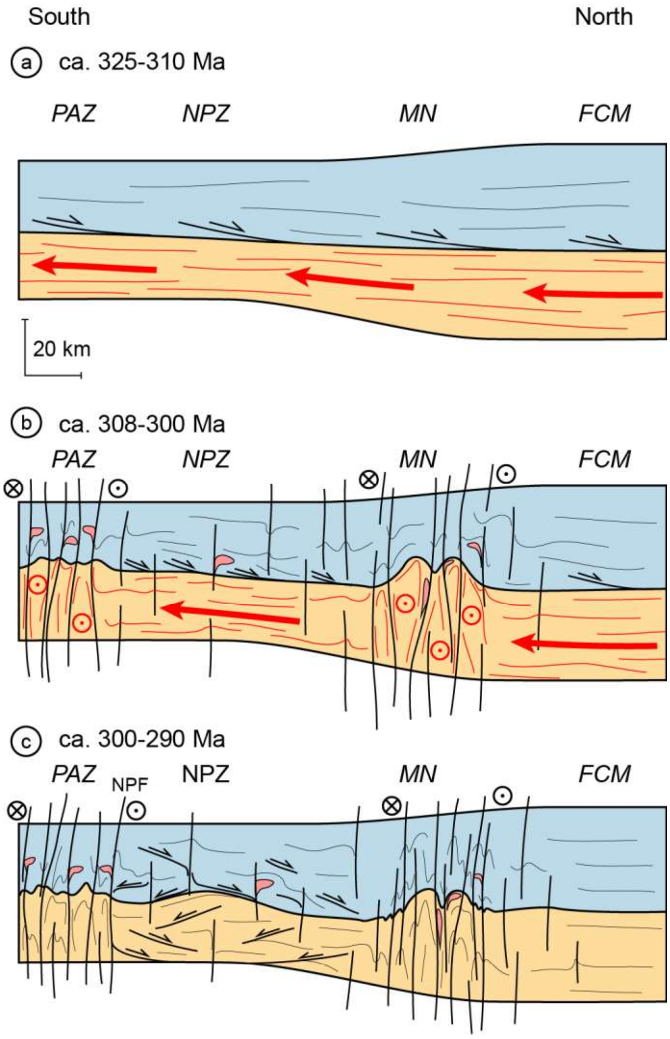
South
North
a ca. 325-310 Ma
PAZ
NPZ
MN
FCM
20 km
b ca. 308-300 Ma
PAZ
NPZ
MN
FCM
c ca. 300-290 Ma
PAZ
NPF
NPZ
MN
FCM

Fig. 17

Table 1

| Sample | Rock type | Structure | GPS location | U-Th-Pb age (±2σ) | |
|---|---|---|---|---|---|
| | | | | **Monazite** | **Zircon** |
| **Samples from S2 strain domains** | | | | | |
| Ag57 | Vivier deformed leucogranite | Infrastructure | N42°46’07’’E02°29’12’’ | 298.9 ± 1.9 Ma | 305.8 ± 6.8 Ma<br>339.5 ± 13 Ma<br>~ 535 - 620 Ma<br>~ 620 - 730 Ma |
| Ag3B (T.S.) | Dam migmatitic paragneiss | Infrastructure | N42°44’51’’E02°35’26’’ | 290.2 ± 1.6 Ma | |
| **Samples from the C2 Shear Zones** | | | | | |
| Ag03 | Undeformed pegmatite | Suprastructure | N42°44’47’’E02°39’44’’ | 290.7 ± 1.5 Ma | 304.6 ± 2.7 Ma |
| Ag38 | Deformed pegmatite | Infrastructure | N42°44’47’’E02°40’06’’ | 291.5 ± 1.6 Ma | 297.6 ± 2.3 Ma |
| Ag47 | Planèze mylonitic pegmatite | Suprastructure | N42°46’07’’E02°37’16’’ | | 299.7 ± 2.7 Ma<br>527.1 ± 9.4 Ma<br>326.6 ± 6.2 Ma |
| **Samples from the Proto-D3 Tournefort area** | | | | | |
| Ag08 | Tournefort undeformed pegmatite | Suprastructure | N42°45’27’’E02°34’12’’ | 296.4 ± 2.4 Ma | 295.5 ± 3.8 Ma<br>323.3 ± 3.8 Ma |
| Ag06 | Tournefort undeformed Leucogranite | Suprastructure | N42°45’54’’E02°34’32’’ | 298.2 ± 2.7 Ma | 298.3 ± 3.2 Ma |
| **Samples from the Late-D3 Tournefort Deformation Zone** | | | | | |
| Ag48 | Vivier Orthogneiss | Infrastructure | N42°46’16’’E02°28’42’’ | 299.7 ± 1.7 Ma | 303.9 ± 5.5 Ma |

| | | | | | |
|---|---|---|---|---|---|
| | | | | | ~ 440 - 480 Ma |
| | | | | | 551.8 ± 4.8 Ma |
| | | | | | 597.2 ± 7.7 Ma |
| Ag51 | Latour de France leucogranite | Infrastructure | N42°45’38’’E02°38’50’’ | 291 ± 2 Ma | 289.4 ± 4.2 Ma |

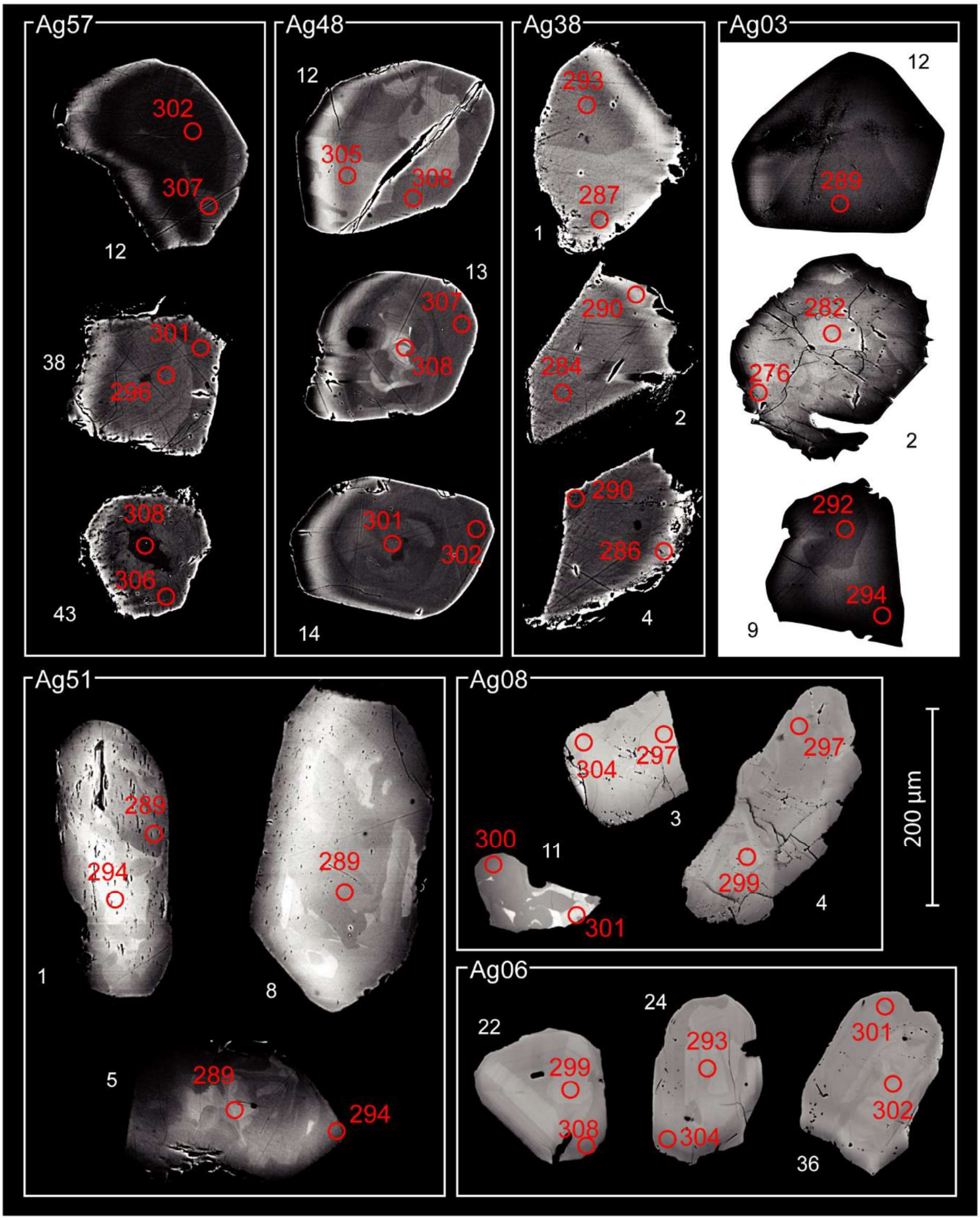
Ag57
302
307
12
301
38
296
308
306
43
Ag48
12
305
308
13
307
308
301
302
14
Ag38
293
287
1
290
284
2
290
286
4
Ag03
12
289
282
276
2
292
294
9
Ag51
289
294
1
289
8
5
289
294
Ag08
304
297
3
297
300
11
299
4
301
200 µm
Ag06
24
22
299
308
293
304
301
302
36

Fig. S1

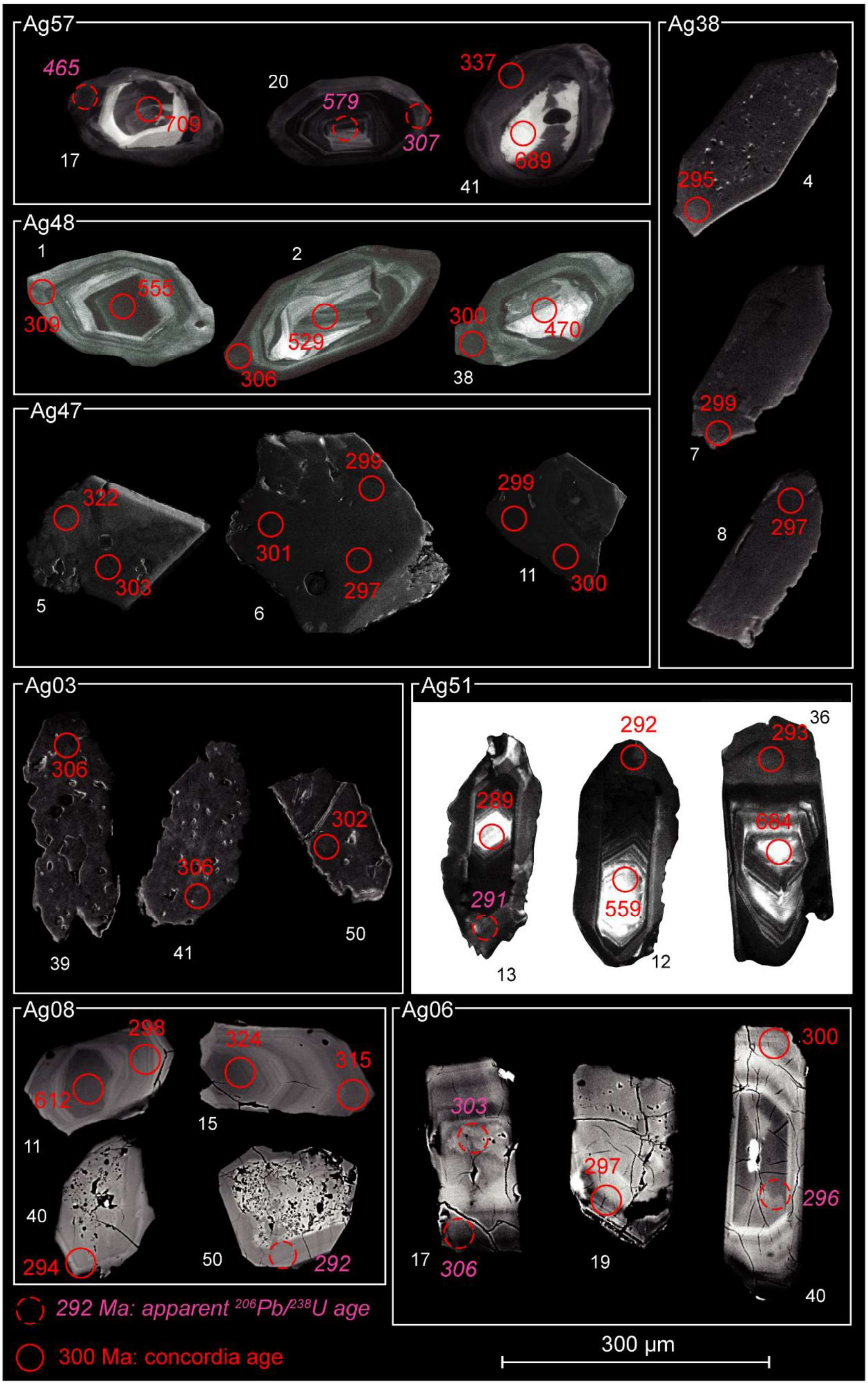
Ag57
465
709
17
20
579
307
337
689
41
Ag38
295
4
299
7
8
297
Ag48
1
555
309
2
529
306
300
470
38
Ag47
322
303
5
299
301
297
6
299
11
300
Ag03
306
39
306
41
302
50
Ag51
289
291
13
292
559
12
36
293
684
Ag08
298
612
11
324
315
15
40
294
50
292
Ag06
303
306
17
297
19
300
296
40
292 Ma: apparent $^{206}Pb/^{238}U$ age
300 Ma: concordia age
300 μm

Fig. S2